



# Modelling platform for control design purposes and large-scale power system studies



This project has received funding from the European Union's Horizon 2020 research and innovation programme under grant agreement No 764011.

# HydroFlex

Increasing the value of Hydropower through increased Flexibility

## D4.1 Modelling platform for control design purposes and large-scale power system studies

<b>Work package</b>	WP4 Flexibility of generator and converter
<b>Task</b>	Task 4.1 Grid interface and grid code adherence and support
<b>Lead beneficiary</b>	University of Strathclyde (USTRAT)
<b>Authors</b>	David Campos-Gaona (USTRAT) Olimpo Anaya-Lara (USTRAT)
<b>Due date of deliverable</b>	30.04.2019
<b>Actual Submission date</b>	30.04.2019
<b>Type of deliverable</b>	Report
<b>Dissemination level</b>	Public

## Executive Summary

The HydroFlex project seeks to increase the flexibility of hydropower and thus provide extended power balancing capabilities in AC grids with large amount of variable renewable energy. In order to increase the flexibility from hydro power, the HydroFlex project enables the variable speed operation of hydro turbines by using a novel generator design and frequency converters based in a back-to-back power electronic topology.

The addition of a power electronic interface between the hydro generator and the AC grid imposes new challenges regarding the fault ride-through capabilities of the flexible hydropower system and its provision of ancillary services. This is because the transient behavior of the flexible hydro system is no longer dictated by the natural response of the hydro generator but instead is the product of a control action from the back-to-back system. In this regard, the present report presents the development of a modelling platform for the design of advance controllers of high power back-to-back converters used to interface hydro generators with the AC grid.

The modelling platform developed in this research is composed of a realistic multi-machine AC grid where different dynamic grid conditions can be simulated. These conditions include frequency excursions of different magnitudes, inter-area oscillations and realistic fault scenarios. The modelling platform also integrates into the grid the model of a back-to-back converter with DC voltage, active and reactive power, and current controllers. A special emphasis in developing a robust set of controllers for the back-to-back converter was made in order to maximize the stability of the system when subjected to the set of dynamic grid conditions simulated by the multi-machine AC grid.

In the future, this modelling platform will be used to develop advanced controllers for the back-to-back converter that will enable the full grid-code compliance of the converter-interfaced hydro generator and the provision of ancillary services in the same manner as a conventional hydro generation system.

Section 1 of this report presents the selection of the electric power system modelling tool, the development of the multi-machine AC system and its operation to simulate different dynamic grid conditions.

Section 2 of this report presents the development of the back-to-back converter and its internal controllers using the two-degrees-of-freedom internal model control approach to maximize robustness.

Section 3 of this report presents simulation results of the interaction of the multi-machine AC system and the back-to-back converter under the full set of dynamic grid conditions that this model can provide.

Section 4 of this report presents the conclusions of this research and future work.

## Table of Contents

Executive Summary.....	3
Table of Contents .....	4
Abbreviations.....	5
1. Development of a realistic multi-machine AC grid.....	6
1.1. Introduction .....	6
1.2. Review of simulation software for model development .....	7
1.3. Grid dynamic condition simulation .....	9
1.3.1. Simulated grid .....	9
1.3.2. Frequency Excursions .....	12
1.3.3. Simulink implementation of AC grid for frequency excursions .....	14
1.3.4. AC Faults .....	17
1.3.5. Simulink Implementation of AC grid for AC Faults .....	18
2. Development of the B2B converter and its robust controllers.....	21
2.1. Structure of the controllers within the B2B converter.....	21
2.2. abc to dq0 Transformation .....	22
2.3. Active and Reactive Power Calculation .....	24
2.4. Active Power Control.....	25
2.5. Reactive Power Control.....	27
2.6. Introduction to IMC Controllers .....	28
2.7. d and q Current Control .....	32
2.8. Direct Voltage Controller .....	33
2.9. Cross Coupling Term Elimination .....	36
2.10. Conversion to Modulator Signals .....	37
2.11. dq0 to abc Transformation .....	38
2.12. Simulink Implementation of the Back to Back converter.....	39
2.13. Steady state simulation of the B2B converter controllers .....	41
3. Dynamic Simulation of the full AC grid.....	44
3.1. Simulation of Frequency Excursions .....	44
3.2. Faults.....	46
4. Conclusions.....	50
5. References .....	51

## Abbreviations

2DF Two degrees of freedom

AC Alternative Current

B2B Back-to-back

DC Direct Current

EMTDC Electro Magnetic Transient Design and Control.

EMTP Electromagnetic Transients Program

GG Generic Generator

GSC Grid Side Converter

HG Hydro Generator

IMC Internal Model Control

MSC Machine Side Converter

PI Proportional Integral

PLL Phase Lock Loop

PSS Power System Stabilizer

PU Per Unit

TG Turbo Generator

# 1. Development of a realistic multi-machine AC grid

## 1.1. Introduction

The ever-increasing inclusion of renewable energies into modern power systems requires extra flexibility without comprising the security of energy provision. In this regard, hydropower, due to its quick response and good ramping capabilities, represents an important asset for the system operators. However, there exist bottlenecks in the usage of hydropower that restrict the number of hydro turbine start-stop and high ramping rates for energy provision.

The HydroFlex project seeks to increase the flexibility of hydropower by enabling a variable speed operation of hydro turbines using a novel generator design and frequency converters based in a back-to-back power electronic topology as seen in Figure 1. This combination not only provides better grid balancing services, but it opens the possibility to use the fast controllers in the power electronic converter interface to provide other ancillary services such as frequency control, reactive power compensation, oscillation damping and increased transient stability of other units in the power system.

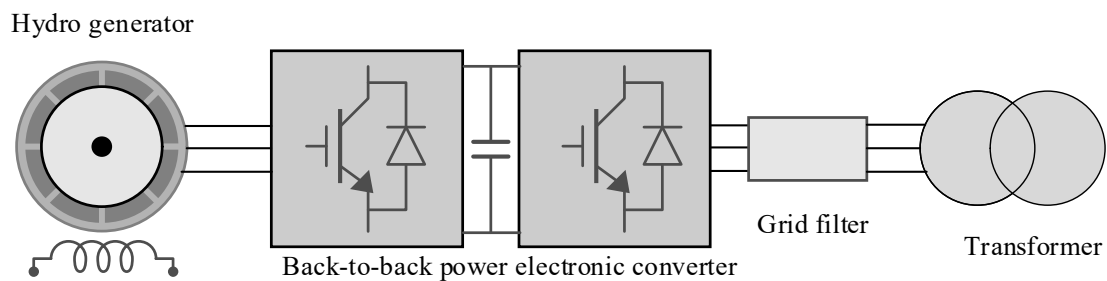


Figure 1: Schematic diagram of a hydro generator connected to the AC grid via a power electronic converter

The design of advance controllers for the power electronic interface is, however, not a straightforward task. The addition of a power electronic interface between the hydro generator and the AC grid imposes new challenges regarding the fault ride-through capabilities of the flexible hydropower system and its provision of ancillary services for the system operators. This is because the transient behavior of the flexible hydro system is no longer dictated by the natural response of the hydro generator but instead is the product of a control action from the back-to-back system. As such, a change in the AC grid frequency will no longer trigger a natural inertia response of from the generator, nor will an AC fault produce the usual fault currents typical of a hydro generator. In this regard, this research seeks to create advanced power electronic controllers that will enable the full grid-code compliance of the converter-interfaced hydro generator and the provision of ancillary services in the same manner as a conventional hydro generation system.

In order to develop the advanced controllers needed for the HydroFlex project, a realistic AC grid simulation platform has been developed as part of this research. The developed modelling platform is composed of a realistic multi-machine AC grid where different dynamic grid conditions can be simulated. These conditions include frequency excursions of different magnitudes, inter-area oscillations and realistic fault scenarios. The modelling platform also

integrates into the grid the model of a back-to-back converter with DC voltage, active and reactive power, and current controllers. A special emphasis in developing a robust set of controllers for the power electronic converter was made in order to maximize the stability of the system when subjected to the set of dynamic grid conditions simulated by the multi-machine AC grid.

In the future, this modelling platform will be used to develop advanced controllers for the back-to-back power electronic converter that will enable the full grid-code compliance of the converter-interfaced hydro generator and the provision of ancillary services in the same manner as a conventional hydro generation system.

### 1.2. Review of simulation software for model development

Model-based computer simulation implements and numerically solves the mathematical equations that define the time behaviour of a physical system and its interactions under steady or changing inputs. In the particular case of the simulation of electric systems, time-domain simulation is common, either using discrete time steps or phasor-based simulation. However, the level of simulation precision and speed differs from different simulation software based in the type of study the software is designed to perform: either power system level phenomena or detail single component operation and phenomena. The time frames of the different electrical phenomena and the type of suitable simulation environment for each is presented in Figure 2.

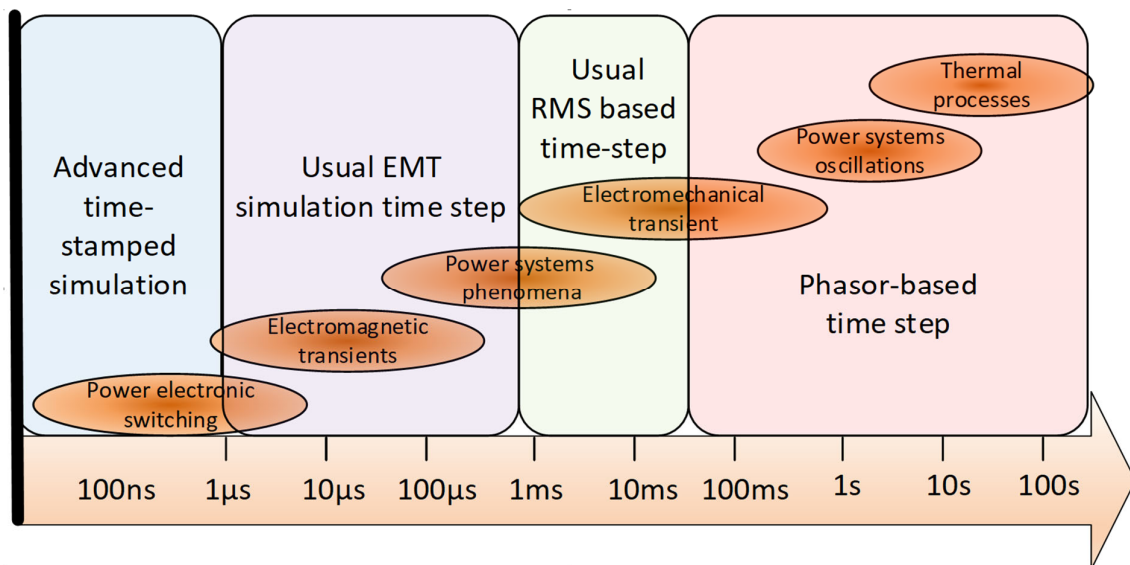


Figure 2: Time frame and usual time step for different type of physical phenomena in the study of power systems

The model developed in this investigation requires a simulation software suitable to study power system phenomena, electromechanical transients and power system oscillations (i.e. sampling times from 50µs to 10s of seconds). Among the wide variety of available software for these types of studies, three commercial simulation software stand out suitable for this project:

*PSCAD/EMTDC* [1]– PSCAD (Power Systems Computer Aided Design) is a graphical user interface to the EMTDC electromagnetic transient simulation engine. PSCAD enables the

user to schematically construct a circuit, run a simulation, analyse the results, and manage the data in a completely integrated, graphical environment. Online plotting functions, controls and meters are also included, enabling the user to alter system parameters during a simulation run, and thereby view the effects while the simulation is in progress. PSCAD comes complete with a library of pre-programmed and tested simulation models, ranging from simple passive elements and control functions, to more complex models, such as electric machines, full-on FACTS devices, transmission lines and cables. If a required model does not exist, PSCAD provides avenues for building custom models. For example, custom models may be constructed by piecing together existing models to form a module, or by constructing rudimentary models from scratch in a flexible design environment.

*DlgSILENT PowerFactory* [2]- PowerFactory is a power system analysis software application for use in analysing generation, transmission, distribution and industrial systems. It covers the full range of functionalities from standard features to highly sophisticated and advanced applications including wind power, distributed generation, real-time simulation and performance monitoring for system testing and supervision. PowerFactory combines reliable and flexible system modelling capabilities with state-of-the-art algorithms and a unique database concept. Also, with its flexibility for scripting and interfacing, PowerFactory is perfectly suited to highly automated and integrated solutions. PowerFactory provides an EMT simulation kernel for solving power system transient problems such as lightning, switching and temporary over-voltages, inrush currents, ferro-resonance effects or sub-synchronous resonance problems, additionally it contains Generic C interface for user-defined controller models.

*Matlab Simulink* - an environment for multi-domain simulation and Model Based Design for dynamic and embedded systems. Simulink contains an additional toolbox, SimPowerSystems, which provides component libraries for modelling and simulating electronic and electrical power systems. It includes models of semiconductors, motors, and components for applications such as smart grids, and renewable energy systems. The simulation can be run at fixed or variable step time simulation of phasor simulation.

Although the spectrum of applications of Matlab is broader than some specialized power system simulators, and its simulation engines are not specifically designed for electric power system simulation, the simPowerSystem toolbox contains enough elements to develop the model of the multi-machine AC grid and implement the dynamic grid conditions with similar results than with more specialized software [3]. Furthermore, the Matlab-Simulink software provides several solvers for electric power systems in both time-based and phasor-based simulation. More important, the control and digital signal processing toolboxes of Matlab makes the software an ideal tool for complex controller deployment, these toolboxes can be fully integrated in the SimPowerSystem environment of Simulink. Power Systems simulation software such as PSCAD and DlgSILENT PowerFactory provide an interface to Matlab Simulink with the purpose of enabling their users the development of controllers in the rich environment of Matlab and Simulink interfaces. As such, given the versatility of Matlab/Simulink, as well as its wide usage worldwide, this project has selected this software to develop the model of the multi machine AC system and the scenarios for different dynamic conditions.

## 1.3. Grid dynamic condition simulation

### 1.3.1. Simulated grid

The AC grid simulated in this report consists of four synchronous machines, transformers, transmission lines and three main loads divided in two power areas by a long interconnector. The total power rating of the grid is of 3.1GW divided in two power areas of 1.6GW and 1.5GW respectively. The grid includes in one of its areas a 100MW B2B converter interfacing a power source regarded as the flexible hydro generator. The power area of the B2B converter has been modelled in higher detail in order to reproduce accurately dynamic grid conditions. As such, the B2B converter power area consists of 3 fully instrumented machines (i.e. including governors, excitation systems and power system stabilizers), two main loads, and the required circuit breakers and parallel lines to implement loss of generation and three phase faults in a realistic manner. The deployment of the grid and the parameters of the interconnector between the two power zones enables the simulation of scenarios with inter-area power oscillations.

Figure 3 shows a schematic diagram of the developed AC grid. As seen in the figure the power area consists of three synchronous machines. Two machines are turbo generators and another machine is a conventional hydro generator. The grid dynamic conditions are created either disconnecting the 600MVA machine from the grid (for frequency excursions) or subjecting one of the parallel transmission lines of the machine to a permanent fault. The faulted line is then disconnected from the circuit using circuit breakers. Since the user has control over the time delay actuation of the circuit breakers, different fault durations can be simulated.

The ratio between generation and load was selected to enable a steady state operative condition where enough spinning reserve is available in case of a loss of generation situation. This prevents the system from collapsing or becoming unstable during dynamic grid conditions. However, all the phenomena associated with a dynamic AC scenario, such as voltage dips, power oscillations and frequency changes affect the system within the grid, including the B2B converter. It is the purpose of this simulation grid to subject the B2B system into realistic dynamic grid conditions for the development of advance controllers.

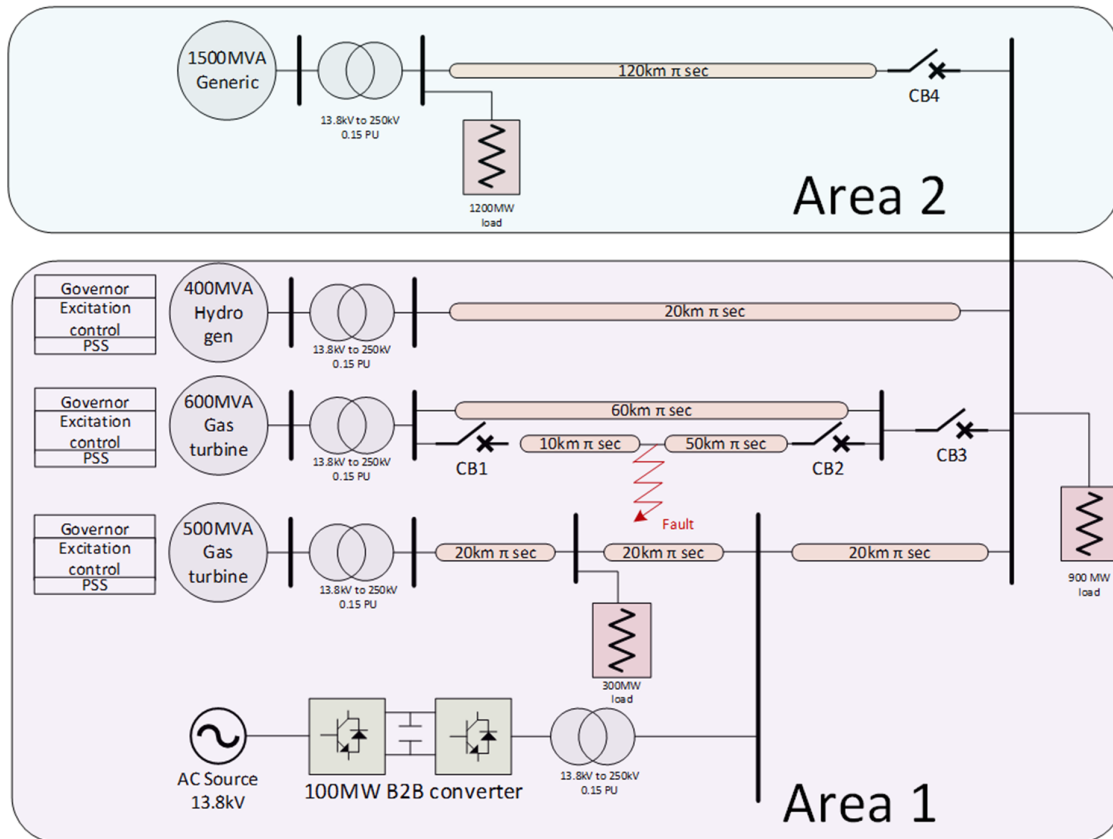


Figure 3: Schematic diagram of the developed AC multi-machine network

Figure 4 shows the developed network in Simulink.

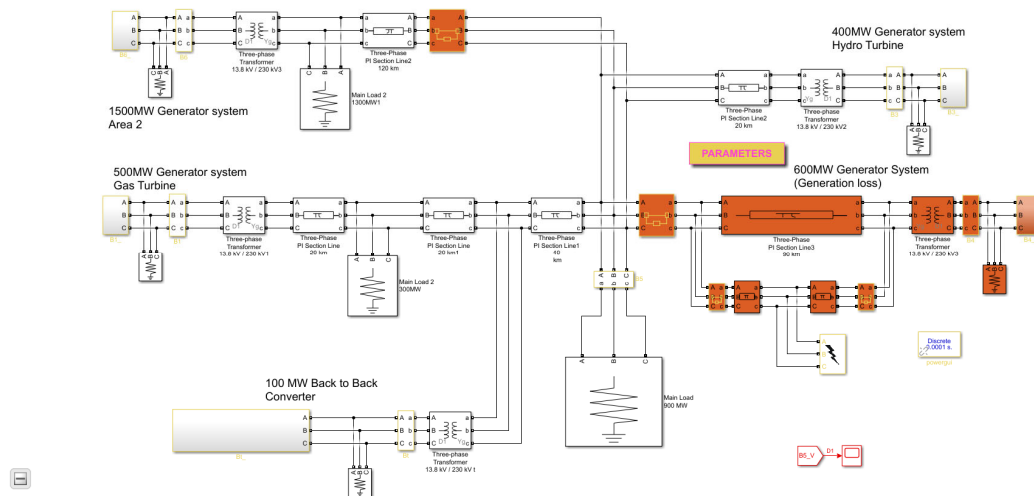


Figure 4: Multi-machine network developed in Simulink

The multi machine AC grid runs from an initial state condition where all the machines are in steady state providing a significant fraction of its power to the grid loads. The initial condition for the multi-machine system was obtained by running power flow analysis. During the power flow analysis, the B2B converter was substituted with a generic 100MW machine

to obtain its steady state of operation and steady state power injection. Once the steady state conditions were obtained, these were embedded within the B2B system resulting in a full steady state operative condition for the simulated grid. The excitation of each machine system was calculated to provide 1 PU of AC Voltage at the terminal of the generator.

The initial steady state power reference for each machine and the B2B converter is shown in Table 1.

*Table 1: Steady state power reference of generators and converters in the simulated AC grid*

<b>Machine and Area</b>	<b>Rated Power</b>	<b>Steady state power reference in PU</b>
<b>Area 1 Hydro Generator</b>	400MVA	0.889858
<b>Area 1 Turbo Generator 1</b>	600MVA	0.698066
<b>Area 1 Hydro Generator</b>	400MVA	0.669803
<b>Area 1 B2B converter</b>	100MVA	0.916192
<b>Area 2 Generic Generator</b>	1500MVA	0.87749

As seen in Table 1, The B2B converter is selected to have an active role in the injection of power to the AC grid, with a steady state power injection of around 90% of its rated power. In this way, any change in its power provision will also have an impact in the dynamics of the grid. This is relevant for advance control derivation.

Figure 5 shows the angular speed of each machine in PU during a period of 5 second simulation. A speed of 1 PU implies the machine is generating power at the rate frequency. As seen in the figure, the speed of all machines in the system is stable and very close to the synchronous speed, with deviation of the level of hundreds of micro PU. This implies the initial conditions calculated for each machine satisfy the steady state performance required for the AC grid. Figure 5 also shows that the fast transient power variation at the start of the simulation produced by the B2B converter produces minimum effect in the frequency of the grid.

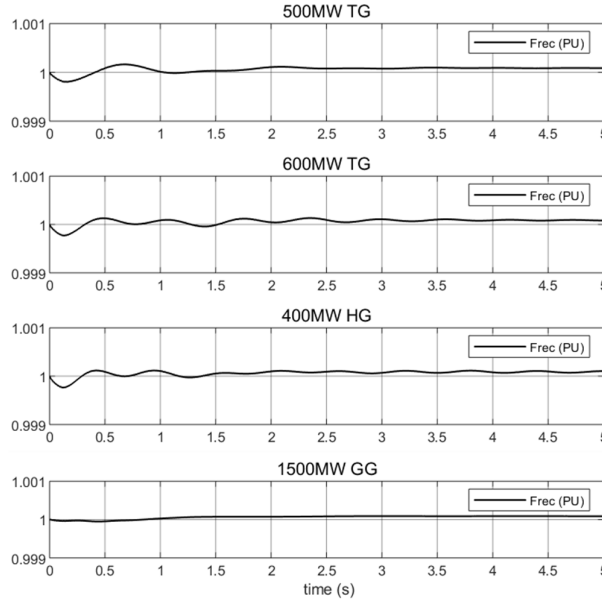


Figure 5: Angular speed of the different machines in the AC network during simulation

Figure 6 shows the result of the simulation of the AC grid with pre-loaded initial conditions. The figure shows the output power (in PU) of the generators and converters connected to the AC grid for the first 5 seconds of simulation. Each subplot corresponds to the power output of an individual machine or the B2B converter. In each subplot the blue line shows the power set point of each generator, in black the actual power delivered by the generator or the B2B is presented. The figure evidences that the pre-loaded steady state of operation and power set point enables a stable simulation. In the case of the B2B converter, its initial power output is 0 but the fast acting controllers within the converter bring the power up to the desired set point in less than 300ms. The initial 0 power production of the B2B converter produces a small disturbance in the rest of the machines, but its magnitude is reduced given the speed of response of the B2B converter controller.

### 1.3.2. Frequency Excursions

In general terms, the frequency behavior of a power grid can be described in a simplified manner with the equation of motion of a single machine rotor. This equation relates the rotor angular position with the interaction of mechanical and electrical torques. The motion equation is given by [4]

$$J \frac{d^2 \theta}{dt^2} = T_m - T_e = T_a \quad (1)$$

where  $J$  is the total moment of inertia of the rotor mass in  $\text{kgm}^2$ ,  $T_m$  is the mechanical torque supplied by the prime mover in N-m,  $T_e$  is the electrical torque output of the alternator in N-m and  $\theta$  is the angular position of the rotor in radians.

Neglecting the losses, the difference between the mechanical and electrical torque gives the net accelerating torque  $T_a$ . In the steady state, the electrical torque is equal to the mechanical torque, and hence the accelerating power will be zero. During this period the rotor will move at synchronous speed  $\omega_s$  in rad/s.

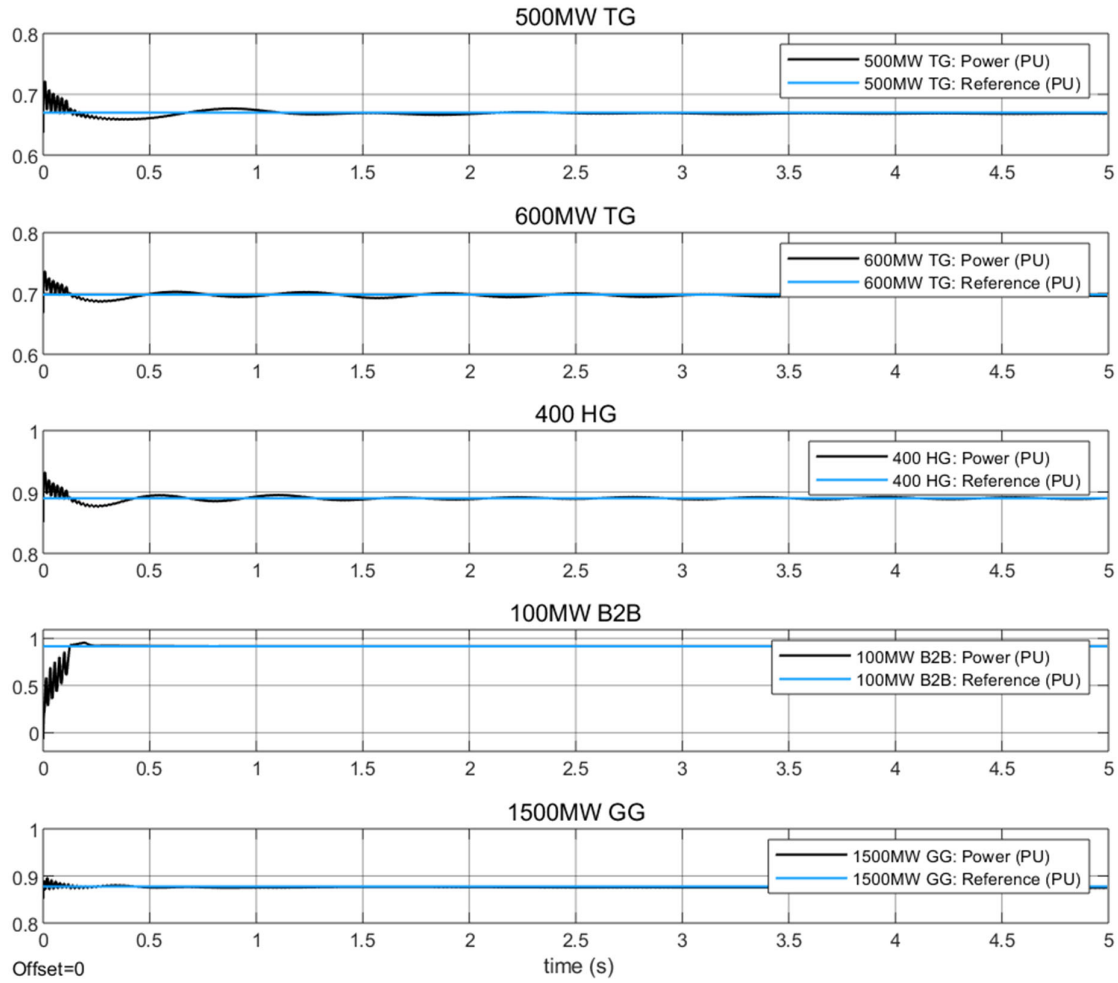


Figure 6: Simulation of power reference vs Power output of machines and converter in the AC grid with pre-loaded initial conditions.

Defining the angular speed of the rotor as

$$\omega_r = \frac{d\theta}{dt} \quad (2)$$

Then the equation of motion can be re-written in terms of rotor angular speed (i.e frequency of the grid) as

$$J \frac{d\omega_r}{dt} = T_m - T_e \quad (3)$$

Equation (3) shows that the rate of change of machine speed is 0 if mechanical and electrical torques are the same. However, in a case where the electrical torque is higher than the mechanical torque, then the rate of change of speed of the machine will be negative and will be dictated by the difference of torques and the amount of the inertia of the system.

If all the machines within the simulated AC grid were aggregated into a single machine expression, then a sudden loss of a generator will be reflected into this single expression as a decrease of  $T_m$  since  $T_e$  represents the electrical loads connected to the AC system and the loss of one generator implies the loss of the  $T_m$  needed to equalise  $T_e$ . A higher  $T_e$  implies a negative rate of change of system frequency. This rate of change is limited by the inertia of the system and is reduced by the actions of the governors of the generators. Although using a single equation to represent the frequency dynamics of a multi machine AC grid is an oversimplification, this equation is still useful to explain the physics behind a frequency excursion in an AC system.

In the specific case of the simulation network developed in this research, a loss of generation is simulated by disconnecting the transmission line connecting to one of the generations of the system, the reasons for this disconnection is simply a command action in the circuit breaker and does not follow a previous faulted stage. However, if required the AC grid can be modified to simulate the fault that leads to the disconnection of the generator. Since this report also contains a section of faults, the analysis of such events will be left for later, and the focus of this section will be the analysis of frequency excursions only.

Since this AC grid is divided in two power areas, there will exist some oscillation between areas, this is typical of large interconnected power systems who regularly show spontaneous, low-frequency power oscillations which are linked to the dynamic stability of those systems. These oscillations can limit the power flow on the interconnected lines between regions of power generation and consumption and even cause instability of the entire power system. The first solution to this problem was to apply damper windings on machines and turbines. Unfortunately, when the power systems started operating close to their stability limits, the weakness of the synchronizing torque available to damp these oscillations were found to be causing system instability. In this regard, a second option to enhance the stability of multi-machine power networks is the implementation of Power System Stabilizers (PSS). The main task of a PSS controller is to provide a damping torque in phase with the oscillation mode in the network, or, in the case of a local oscillation, in phase with the concerned machine. The IEEE structure of a “conventional” PSS consists of a gain and a phase correction[5]. By correctly tuning these gains and compensators the oscillations of a synchronous machine can be compensated irrespective of its mechanical torque control. This is because the output signal from the “PSS” is injected into the voltage regulator of the machine, where it acts on the excitation voltage.

If a magnified effect of this oscillations is required, the PSS of the generators can be disabled allowing the frequency of the grid to oscillate following the power oscillation within areas. This type of behaviour is beneficial to test the robustness of the B2B controllers and its ability to synchronize with an AC grid during extreme frequency excursions.

### 1.3.3. Simulink implementation of AC grid for frequency excursions

In order to trigger the model to produce a frequency excursion, the circuit breaker at the transmission line connecting the 600MVA turbo generator must be enabled. When enabled this circuit breaker opens the connection at  $t=5s$  by default. Figure 7 shows the location within the Simulink model of the circuit breaker that triggers the loss of generation event.

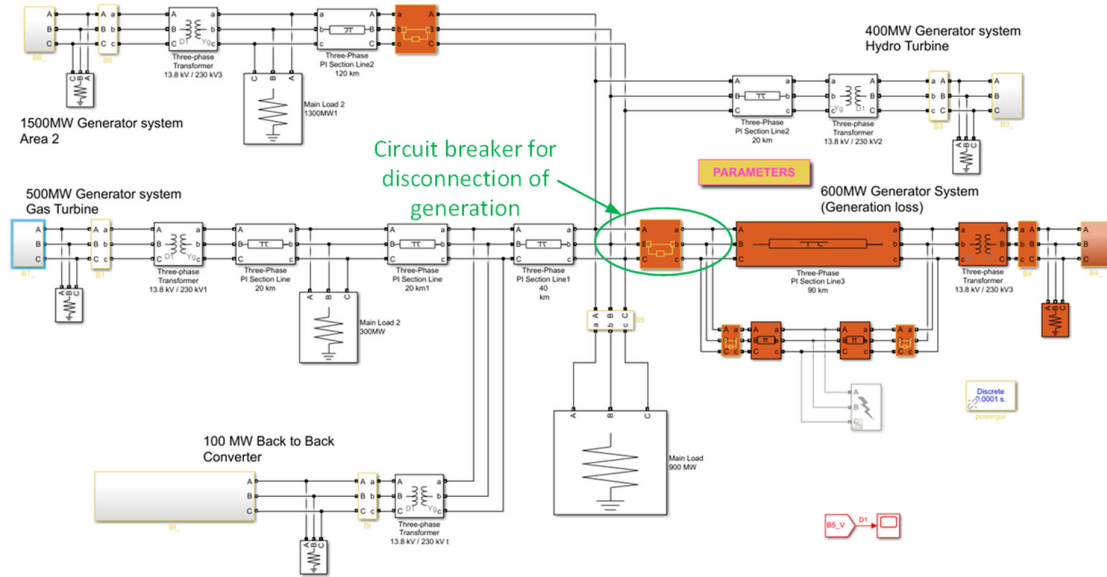


Figure 7: location of the circuit breaker used to generate a loss of generation scenario in the AC grid

Figure 8 shows the power behaviour of the generators and converter during the loss of generation event for a case of reduced oscillations (figures a to e) and for a case of increased oscillations (figures f to j).

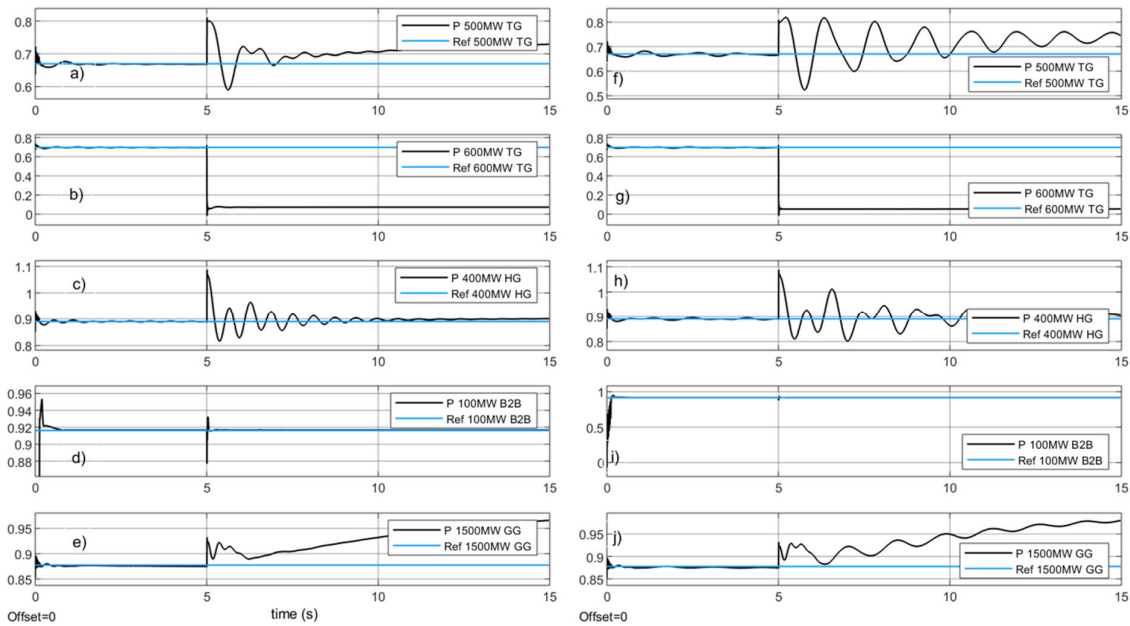


Figure 8: Multi-machine network under a case of loss of generation. a) power output of the 500MW turbo generator (PSS on), b) power output of the 600MW turbo generator (PSS on) c) power output of the 500MW hydro generator (PSS on) d) power output of the 100MW B2B (PSS on) e) power output of the 1500MW generic generator (PSS on), f) power output of the 500MW turbo generator (PSS off), g) power output of the 600MW turbo generator (PSS off), h) power output of the 500MW hydro generator (PSS off) i) power output of the 100MW B2B (PSS off) j) power output of the 1500MW generic generator (PSS off)

As seen in Figure 8b) and g), at the instant the loss of generation happens, the power output of the disconnected generator collapses. For the rest of the generators its natural response

is to release kinetic energy to oppose to the change of frequency, this is seen as a large spike of power in the rest of the generators output just after the generation loss. The loss of generation even produces inter-oscillations between the generators in area 1 and between areas as well. For the case where these oscillations are reduced using PSS (figures a to e), it is noticed that after the initial release of kinetic energy the remaining connected generators gradually adjust their power output to compensate for the missing power of the disconnected generator. This is purely the action of the governor of the generators. For the case where these oscillations are not reduced (PSS are disabled in generators, figures f to j) it is noticed that after the initial release of kinetic energy the remaining connected generators also being gradually adjust their power output to compensate for the missing power of the disconnected generator but much larger oscillations are present in the operation of the generators. Something interesting to notice is that the power output of the B2B converter remains unchanged during the loss of generation, and that the oscillations in power of nearby generators do not affect its capability to inject power or to synchronize with the AC network. Although this will be reviewed in detail later, the B2B converter controllers are robust enough to ride through frequency excursions and voltage fluctuations product of inter area power oscillations.

Figure 9 a) to d) shows the angular speed of each generator in PU using PSS. Figure 9 e) to h) shows the angular speed of each generator in PU without the use of a PSS to damp oscillations. A value of 1 PU implies a synchronous speed of 50Hz.

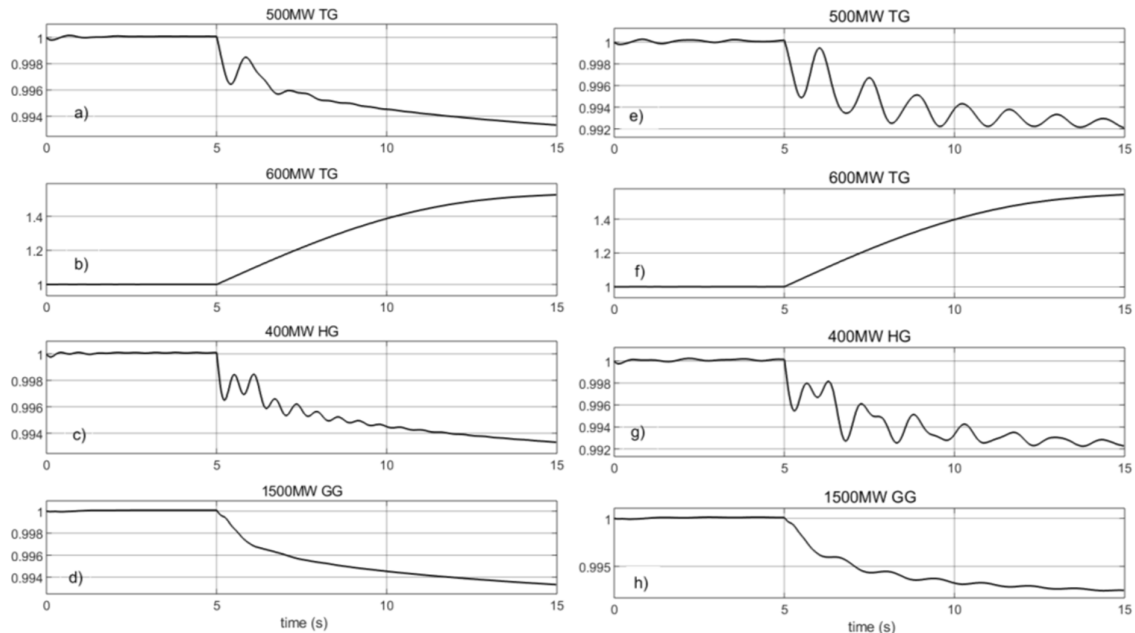


Figure 9: Angular speed of generators during a loss of generation event. a) angular speed of the 500MW turbo generator (PSS on) b) angular speed of the 600MW turbo generator (PSS on), c) angular speed of the 400MW hydro generator (PSS on), d) angular speed of the 1500MW generic generator (PSS on), e) angular speed of the 500MW turbo generator (PSS off) f) angular speed of the 600MW turbo generator (PSS off), g) angular speed of the 400MW hydro generator (PSS off), h) angular speed of the 1500MW generic generator (PSS off).

As seen in Figure 9 b) and f), the action of the circuit breaker leads to the disconnection of the 600MW turbo generator which speeds up uncontrollably. For the rest of the generators

in the system the loss of generation implies a reduction of its angular speed. In the case of Figure 9 a) b) and d) (i.e. PSS on), the speed reduction follows the same pattern in all the generators since they are all synchronized, however the power oscillation in area 1 produce minimum changes in the individual angular speed of each generator. For the case of the generator in area 2 (figure d), there are no oscillations and the frequency droops smoothly following the dynamics of equation (3).

In the case of Figure 9 e) f) and h) the PSS action is disabled which leads to large speed oscillations of each generator after the loss of generation event. The oscillations are more evident in the machines of area 1 (figures e and f) and in lesser degree in the machine in area 2 (figure h). Although the magnitude of these angular speed oscillation has been artificially magnified by disabling the PSS of the multi-machine AC grid, they are useful to test in a simulation environment the robustness of synchronization and power controllers of the B2B converter.

#### 1.3.4. AC Faults

A short circuit can be defined as an abnormal connection of very low impedance between two points of different potential, whether made intentionally or accidentally. These are the most common and severe kind of faults, resulting in the flow of abnormal high currents through the elements of the power system or transmission lines. If these faults are allowed to persist even for a short period, it leads to the extensive damage to the elements of the power system.

When a short circuit happens, the voltage of the grid suffers a reduction or a dip in its magnitude, the dip magnitude during a fault depends on the impedance of the fault and the impedance of the source. To illustrate this, a simple model consisting of one generator and 1 load is presented in Figure 10.

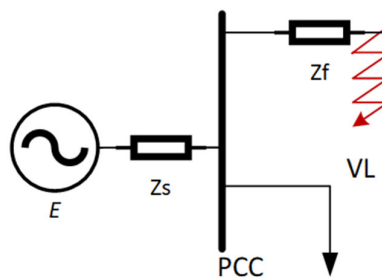


Figure 10: Radial AC system to calculate a voltage dip in the common

The model presented in the figure is only valid for a radial system where the bus is only fed from a single source. In this model the voltage at the load  $V_L$  will be result of a voltage divider between the fault impedance  $Z_f$  and the source impedance  $Z_s$ , this is:

$$V_L = E \frac{Z_f}{Z_s + Z_f} \quad (4)$$

As indicated by (4) a higher value of  $Z_c$  (i.e. a weak grid) the magnitude of the dip will increase for a given value of a fault impedance. Additionally a smaller value of  $Z_f$  (a stronger fault) will also increase the magnitude of the dip.

The model presented in Figure 10 is not valid for meshed systems, which will require the use of node impedances/admittance matrices to obtain the solution. However, it is used to illustrate the basic relationship between fault impedance, grid impedance and voltage dip.

### 1.3.5. Simulink Implementation of AC grid for AC Faults

In order to trigger the Simulink model to produce a voltage dip, a short circuit in the middle of one of the parallel transmission lines connecting the 600MVA turbo generator was implemented. When enabled the short circuit produces a 3-phase fault at  $t=5s$  by default. The magnitude of the short circuit impedance can be modified by the user. The duration of the short circuit is defined by the disconnection timing of the circuit breakers at the ends of the faulted line. As a default the circuit breakers isolate the fault after 3 cycles of the fundamental, however this also can be modified by the user. Figure 11 show the location of the fault in the Simulink model.

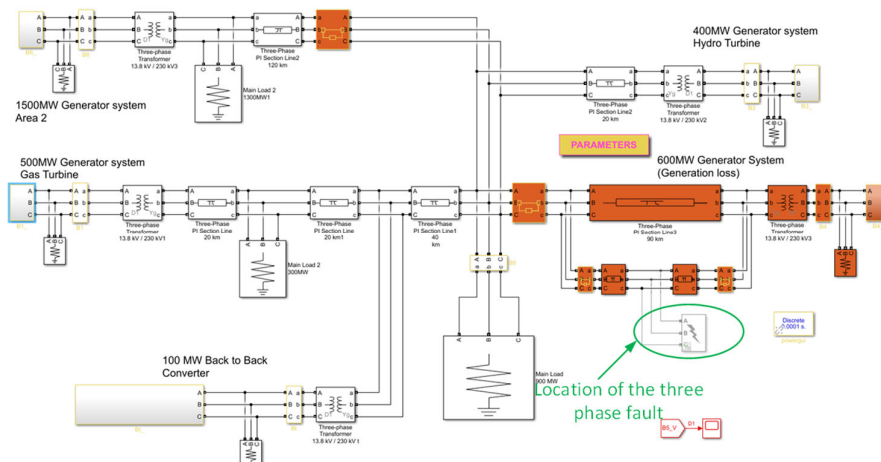


Figure 11: Location of the short circuit used to generate a voltage dip in the AC network

Figure 12 shows the power behaviour of all machines and the converter during the voltage dip, in this simulation a short circuit impedance was selected in order to subject the power grid to a 0.5 magnitude voltage dip for 3 cycles of the fundamental. Figure 12 f) shows the voltage profile at the terminals of the main load.

As seen in Figure 12 a) b) c) and e) the fault produces a transient spike in power output in all machines, this is due the transient current output of the machines during a three-phase fault event. Shortly after the power spike the power output of the machines moves to a new operative value during the fault happening, however after the faulted line is isolated, the machines return to their pre-fault power output level. Some machines are affected by power oscillations; however, these oscillations are readily damped by the PSS of the machines.

Figure 12 d) shows the power output of the B2B converter, since the current behaviour of the converter is not dictated by a transient characteristic, such as it is in generators, but is regulated by a control loop, there is not a transient current peak out of the B2B converter at

the moment of the fault. Rather, the power injection capacity of the B2B converter gets limited by the limited voltage magnitude, this is reflected as a drop in the power provision of the B2B converter as seen in Figure 12d). After the fault is isolated and the voltage levels of the grid are restored the B2B converter is seen injecting to the grid a power level beyond its set point value. This is because all the power input to the B2B converter remained constant during the fault period. Since the B2B converter could not deliver to the grid all its incoming power, part of this power charged the DC capacitors of the B2B link with extra energy. In order to discharge the capacitors from this extra power, the B2B delivers extra power to the grid until all the excess of energy in the DC capacitors is removed. Here it is important to mention that the excess of energy in DC capacitors increases the magnitude of the voltage in the DC link. In real world systems the DC voltage cannot be allowed to increase beyond the rated value of the DC capacitors, because of this, it is necessary to provide with the B2B converter with protection and control measurements to protect the integrity of the capacitors during fault periods. In later sections of this report, this issue and possible solutions will be analysed with more detail.

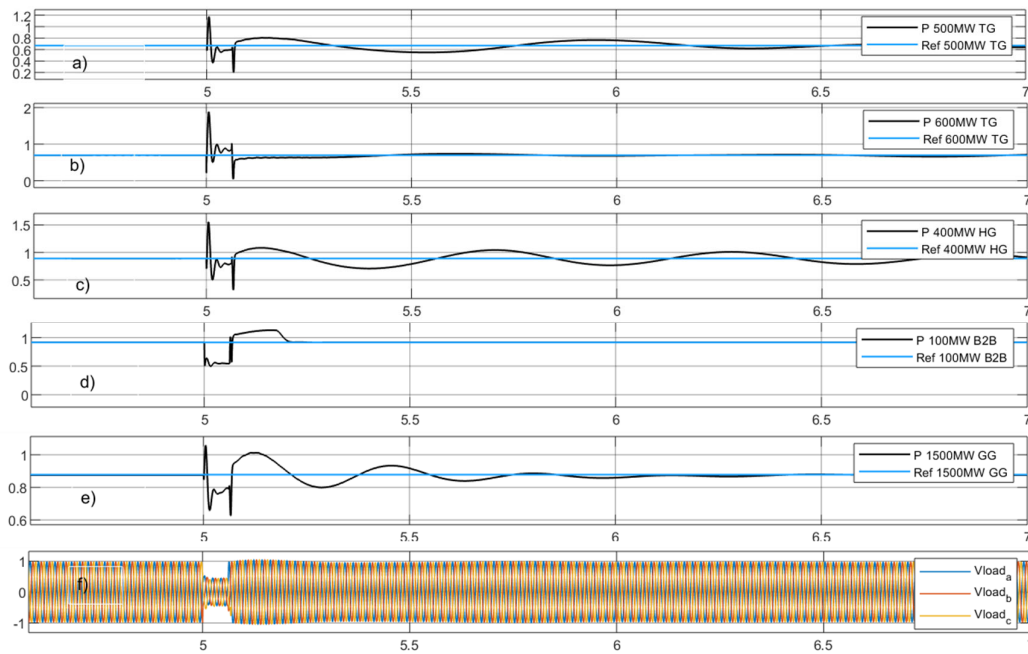


Figure 12: Behaviour of the AC grid during a 3-phase fault. a) 500MW turbo generator, b) 600MW turbo generator, c) 400 MW hydro generator, d) 100MW B2B converter, e) 1500 MW generic generator, f) grid voltage in PU at the terminals of main load 1.

Figure 13 shows the behaviour of the angular speed of all generators during the fault happening

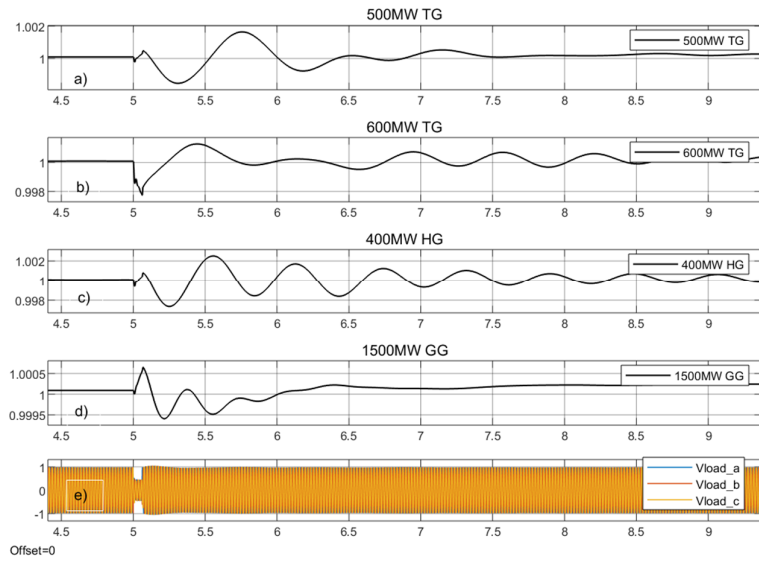


Figure 13: Angular speed behaviour during the three-phase fault. a) 500MW turbo generator, b) 600MW turbo generator, c) 400MW Hydro generator, d) 1500MW generic generator e) voltage profile at the terminals of main load 1

## 2. Development of the B2B converter and its robust controllers

### 2.1. Structure of the controllers within the B2B converter

The B2B converter consists of two voltage source converter (VSC) interconnected via a common DC link. Each VSC consist of a 2-level three phase converter. The converter connected to the hydro generator is named the Machine Side Converter (MSC) whereas the converter connected to the AC grid is named Grid Side Converter (GSC). For a proper functioning of a B2B converter the MSC and GSC should work in a coordinated manner where whatever energy is injected to the MSC by the Hydro generator should be the same energy that the GSC converter delivers to the AC grid.

Figure 14 shows a schematic diagram of the 2 level 3-phase B2B converter designed to interface the flexible hydro generator with the AC grid. As seen in the figure, the B2B converter consist of two 6-IGBT VSCs connected by a DC bus, a DC capacitor and a grid filter. Each converter has its individual controllers.

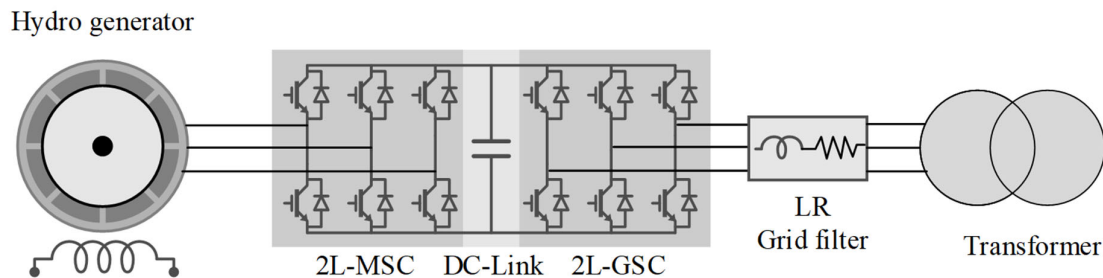


Figure 14: Schematic diagram of the B2B converter interfacing the flexible Hydro generator with the AC grid

The B2B converter is capable to produce an AC voltage simultaneously at the MSC and GSC by the action of the power electronic switches. The AC current can flow in any direction (i.e. positive or negative) with respect of the voltages of the converter. The magnitude and direction of the currents with respect of the voltage of the GSC or MSCs will define if the VSC converters are working in a rectifiers/inverter configuration or vice versa.

In the case of the flexible hydro generator, the MSC will usually work as a rectifier, i.e. the AC power from the generator will be rectified as DC power which is transmitted to the GSC via the DC link. The GSC will usually work as an inverter where the DC power in the DC link will be converted to AC power and delivered to the grid.

The coordinated functioning of the MSC and GSC is achieved by controlling the voltage in the DC capacitor of the DC link. This voltage is an indicator of the energy balance between MSC and GSC. If the voltage of the DC link is kept constant by control of one of the VSC converters, then whatever power enters the DC link will be delivered as AC power in the converter working as an inverter. This is because the voltage in the capacitor is an indicator of the energy stored in the DC link. If the power that enters the DC link is the same as the power that leaves the DC link, then the voltage of the capacitor does not change. However, if

there is imbalance between the rectified power and the inverted power, then voltage of the DC link will change with respect of this imbalance. The converter in charge of controlling the DC voltage does so by changing the amount of energy that the converter extracts or injects to the DC link. Thanks to this configuration the converters of a B2B can work in a coordinated manner without external communications.

Given the small capacity of the DC capacitors to absorb energy for extended periods of time, it is necessary that the controller in charge of regulating the DC voltage acts in a fast manner to avoid an excessive energy storage (i.e. excessive voltage) condition in the capacitor. The response time of this type of controllers should be in the range of 10s of milliseconds for the B2B to function properly. Knowing this, the design of the voltage and current controllers of the B2B converter is a non-trivial task, especially when other grid conditions, such as frequency excursions or voltage sags have the possibility to affect the stability of fast controllers.

Figure 15 shows the different controllers and subsystems that define the functioning of the B2B converter, the functioning of each subsystem will then be described in detail in the next section of this report.

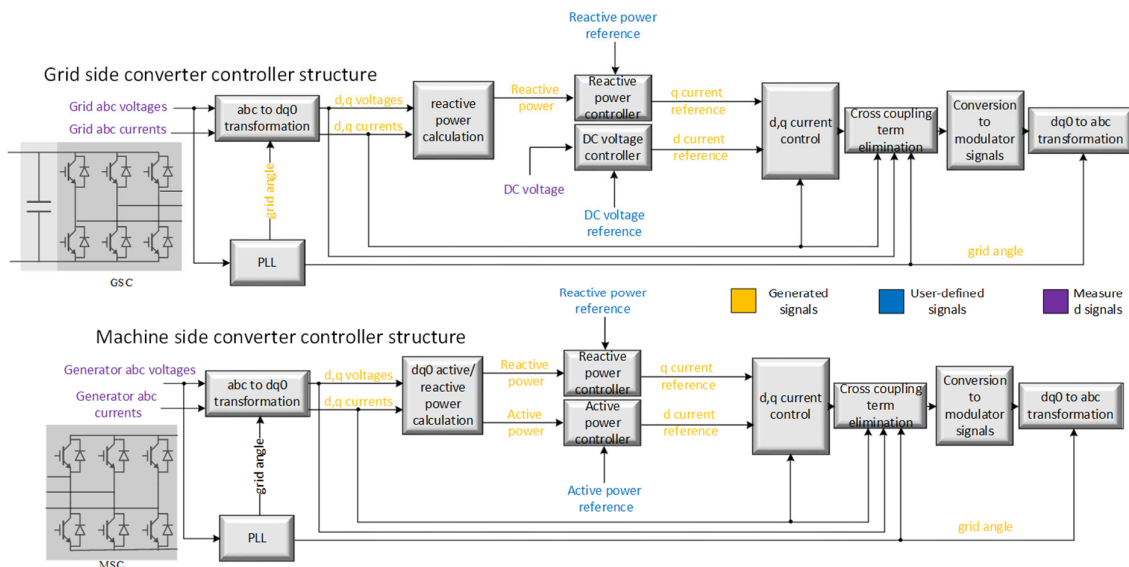


Figure 15: Controller structure of the MSC and GSC converters of the B2B system

## 2.2. abc to dq0 Transformation

It is well-known that for a PI or IMC controllers, zero steady state error between the set point and the steady state signal is achieved as long as set point and the signal-to-control are DC quantities in steady state. However, the control of the AC currents of the VSCs is instrumental for carrying out all the rest of the control objectives of the B2B converter. Since the signals-to-control are in this case a set 3 sinusoidal signals, PI controllers are incapable to regulate these currents without a steady state phase error. To alleviate this problem, a mathematical transformation that converts 3 phase AC quantities into 3 DC quantities is used. This transformation converts a three-phase time-domain signal from a stationary coordinate system, *abc*, to a rotating coordinate system of two orthogonal phases *d*, *q* and a

zero sequence component. The  $q$  axis of the  $dq0$  coordinate system is chosen to be lagging the  $d$  axis by 90 degrees. The angular speed of the  $dq0$  rotating coordinate system can be chosen to match the synchronous speed of the AC grid; this allows to mathematically “see” any AC voltage or current space vector that is rotating at the same angular speed to that of the  $dq0$  frame as a constant spatial distribution[6]. Hence, any balanced three-phase ac space vector quantities can be transformed to two DC quantities (resulting from the projection of the ac space vector in the  $d$  and  $q$  axis) and a zero-sequence component. Figure 16 shows the geometric derivation of the  $dq0$  transformation applied to the three-phase waveform where  $\theta_{dq}$  is the angle between the  $d$  axis of the rotating frame and phase  $a$  of the three phase system,  $\omega_s$  is the angular speed of the three-phase system and  $\omega_{dq}$  is the angular speed of the  $dq0$  rotating frame.

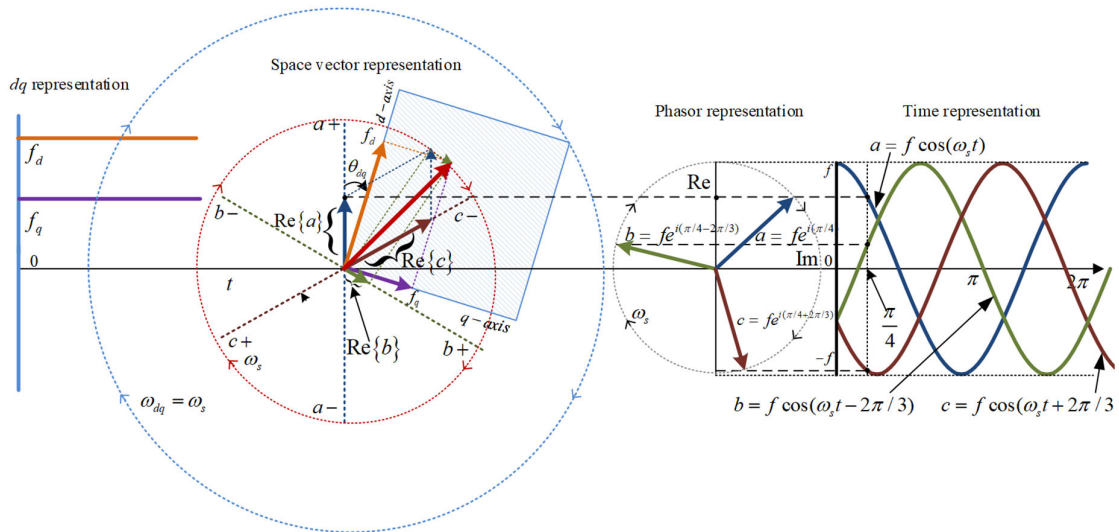


Figure 16: Geometric Derivation of the  $dq0$  Transformation applied to a 3-Phase System

The  $dq0$  transformation is performed to the grid voltages by applying the following transformation the 3-phase voltage signal:

$$\begin{bmatrix} v_d \\ v_q \\ v_0 \end{bmatrix} = \frac{2}{3} \begin{bmatrix} \cos \theta_{dq} & \cos(\theta_{dq} - \frac{2\pi}{3}) & \cos(\theta_{dq} + \frac{2\pi}{3}) \\ -\sin \theta_{dq} & -\sin(\theta_{dq} - \frac{2\pi}{3}) & -\sin(\theta_{dq} + \frac{2\pi}{3}) \\ \frac{1}{2} & \frac{1}{2} & \frac{1}{2} \end{bmatrix} \begin{bmatrix} v_a \\ v_b \\ v_c \end{bmatrix} \quad (5)$$

where  $v_d$ ,  $v_q$  and  $v_0$  are the  $d$ ,  $q$  and 0 representation of the grid voltage respectively,  $v_a$ ,  $v_b$  and  $v_c$  are the  $a$ ,  $b$  and  $c$  grid voltages and  $\theta_{dq}$  is a function of  $\omega_{dq}$  and of an initial value  $\theta_{dq}(0)$ :

$$\theta_{dq} = \int_0^t \omega_{dq}(t) dt + \theta_{dq}(0) \quad (6)$$

The calculation of the  $d$ ,  $q$ , and 0 grid currents  $i_d$ ,  $i_q$  and  $i_0$  from the a, b, c currents  $i_a$ ,  $i_b$  and  $i_c$  is carried out using the same transformation presented in (5).

Given the type of connection of a VSC and the grid source, the zero-sequence voltages and currents are zero by physical constraints, no matter if the phases are balanced or not. As such, the  $dq0$  representation of the grid voltages and currents can be reduced to a  $dq$  without losing information. Because of this, the zero-sequence representation of the voltage and currents are disregarded for controller design purposes.

If in the dq0  $\omega_{dq}$  is selected to be  $\omega_{dq} = \omega_s$  then the transformation will be synchronized with the AC grid and the dq0 values will become DC quantities, as such PI or IMC controllers can be used to generate fast and robust controllers able to control the magnitude and phase of the 3 phase AC system with zero steady state error.

In order to synchronize the dq0 transformation with the AC grid, a system that provides the transformation with  $\omega_s$  is required. This is the task of the Phase Lock Loop (PLL).

The PLL A phase-locked loop or phase lock loop (PLL) is a control system that generates an output signal whose phase is related to the phase of an input signal. A useful analogy for the PLL behaviour consists of a servo motor that tries to catch a rotating mass. The angle provided by the PLL output is synchronized with the positive sequence of the filtered grid voltage. The PLL measures the alpha and beta components of the voltage and translates them to the dq-reference frame. If the dq-frame is fully aligned with the alpha component, the angle of the voltage vector should be ideally zero. If the dq-frame is not fully aligned there is an error, and the angle of the voltage vector in the dq-reference frame will not be zero. The closed loop control will try to increase/decrease the reference frame angular speed to make that angle null. For this aim, the PLL passes the angle error through a PI controller. The output of this PI controller is the angular speed (frequency) of the rotating dq-reference frame. The phase of the dq-reference frame is obtained by using an integrator (a VCO in a traditional PLL) for the previous frequency. The PLL used in this research is the well-known robust SOGI PLL [7].

### 2.3. Active and Reactive Power Calculation

The apparent power of a 3 phase AC system,  $S$ , in terms of  $dq$  voltages and currents is defined as:

$$\begin{aligned} S &= \frac{3}{2}(v_{dq})(i_{dq})^* = \frac{3}{2}(v_d + jv_q)(i_d - ji_q) \\ &= \frac{3}{2}(v_d i_d + v_q i_q) + j(v_q i_d - v_d i_q) = P + jQ \end{aligned} \quad (7)$$

where  $P$  is the active power and  $Q$  is the reactive power. If the  $d$  axis of the  $dq0$  rotatory frame is assumed to be aligned with the ac space vector, then the voltage representation in  $dq$  consist only of  $d$  components (i.e.  $\omega_{dq} = \omega_s$ ,  $v_d = v_s$  and  $v_q = 0$ ) as seen in Figure 17. In this case, equation (7) can be simplified to

$$P = \frac{3}{2} v_d i_d$$

$$Q = -\frac{3}{2} v_d i_q$$
(8)

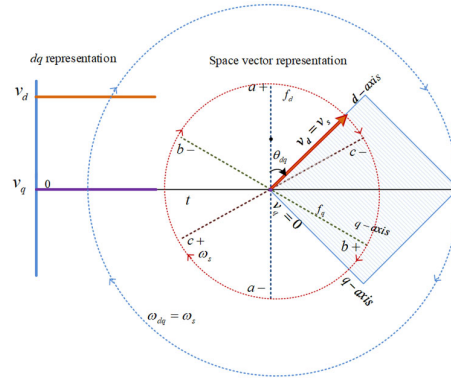


Figure 17: dq0 Transformation of the Grid Voltages when the d Axis is aligned to the AC Space Vector

## 2.4. Active Power Control

According to equation (8), the relationship between the amount of  $d$  current and the inverter active power is directly proportional (assuming constant AC voltage). Because of this, a simple integral controller is enough to control the active power with first order dynamics and 0 steady state error. The transfer function,  $G_p$ , from the active power  $P$  to the  $i_d$  current is given by

$$G_p = \frac{i_d}{P} = \frac{2}{3v_d} \quad (9)$$

If an integral controller of the type  $C_p(s) = Ki_p / s$ , (where  $Ki_p$  is the integral constant of the active power controller and  $s$  is the Laplace variable) is added in cascade with  $G_p$  the following open loop expression is obtained:

$$A_p(s) = G_p \cdot C_p(s) = \frac{2Ki_p}{3v_d s} \quad (10)$$

If  $Ki_p$  is selected to have a value of  $Ki_p = 3v_d \alpha_p / 2$ , where  $\alpha_p$  can be regarded as the closed loop bandwidth of the controller, then the open loop expression  $A_p(s)$  and the closed loop expression  $E_p(s)$  from the active power reference  $P_{ref}$  to  $P$  are:

$$A_p(s) = \frac{2}{3v_d s} \frac{3v_d \alpha_p}{2} = \frac{\alpha_p}{s} \quad (11)$$

$$E_p(s) = \frac{P}{P_{ref}} = \frac{A_p(s)}{1 + A_p(s)} = \frac{\alpha_p}{s + \alpha_p} \quad (12)$$

As seen in equation (12), the closed loop dynamics of the active power control loop are first order with a closed loop bandwidth of  $\alpha_p$ . The value of  $\alpha_p$  can be selected for a given rise

time of the control variable by following the formula that defines the relationship between bandwidth and rise time in first order systems. This formula is given by [8]:

$$\alpha_p \approx \frac{0.35}{t_{r\_p}}(\text{Hz}) \text{ or } \alpha_p \approx \frac{2.2}{t_{r\_p}}(\text{rad}) \tag{13}$$

where  $t_{r\_p}$  is the desired rise time of the closed loop system. Figure 18 shows the block diagram of the active power control loop

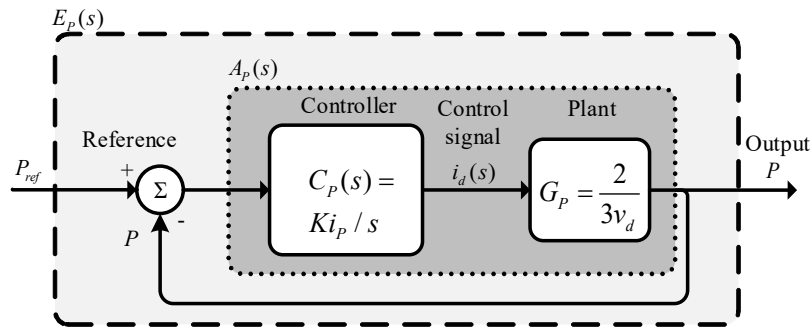


Figure 18: Schematic Diagram of the Active Power Control Loop

Figure 19 shows the digital implementation of the active power controller where  $T_s$  is the sampling time.

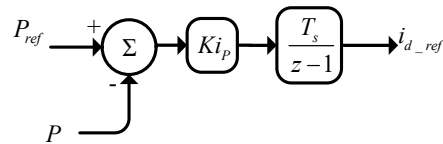


Figure 19: Digital Implementation of the Active Power Controller

Figure 20 shows the step response and the bode plot of active power closed loop control system for a bandwidth of  $\alpha_p = 220$  rad. ( $t_{r\_p} = 0.01$  sec).

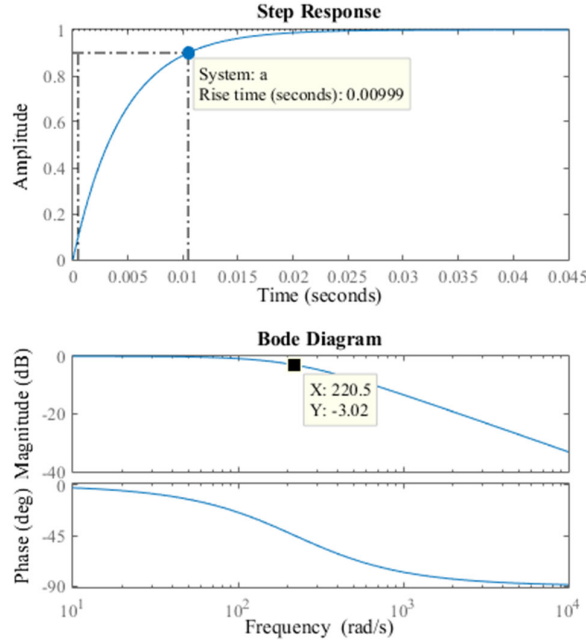


Figure 20: Step response and bode plot of the closed loop active power controller

## 2.5. Reactive Power Control

According to equation (8), the relationship between the amount of  $q$  current and the inverter reactive power is directly proportional if the ac voltage is assumed to be a constant value. Because of this, a simple integral controller is enough to control the reactive power with first order dynamics and 0 steady state error. The transfer function,  $G_Q$ , from the reactive power  $Q$  to the  $i_q$  current is given by

$$G_Q = \frac{i_q}{Q} = -\frac{2}{3v_d} \quad (14)$$

If an integral controller of the type  $C_Q(s) = Ki_Q / s$ , (where  $Ki_Q$  is the integral constant of the reactive power controller) is added in cascade with  $G_Q$  the following open loop expression is obtained:

$$A_Q(s) = G_Q \cdot C_Q(s) = -\frac{2Ki_Q}{3v_d s} \quad (15)$$

If  $Ki_Q$  is selected to have a value of  $Ki_Q = -3v_d \alpha_Q / 2$ , where  $\alpha_Q$  can be regarded as the closed loop bandwidth of the controller, then the open loop expression  $A_Q(s)$  and the closed loop expression  $E_Q(s)$  from the reactive power reference  $Q_{ref}$  to  $Q$  are:

$$A_Q(s) = -\frac{2}{3v_d s} \left( -\frac{3v_d \alpha_Q}{2} \right) = \frac{\alpha_Q}{s} \quad (16)$$

$$E_p(s) = \frac{Q}{Q_{ref}} = \frac{A_Q(s)}{1 + A_Q(s)} = \frac{\alpha_Q}{s + \alpha_Q} \quad (17)$$

As seen in equation (17) the closed loop dynamics of the active power control loop are first order with a closed loop bandwidth of  $\alpha_Q$ . The value of  $\alpha_Q$  can be selected for a given rise time of the control variable by following the formula that defines the relationship between bandwidth and rise time in first order systems. This formula is described in (13).

Figure 21 shows the block diagram of the reactive power control loop.

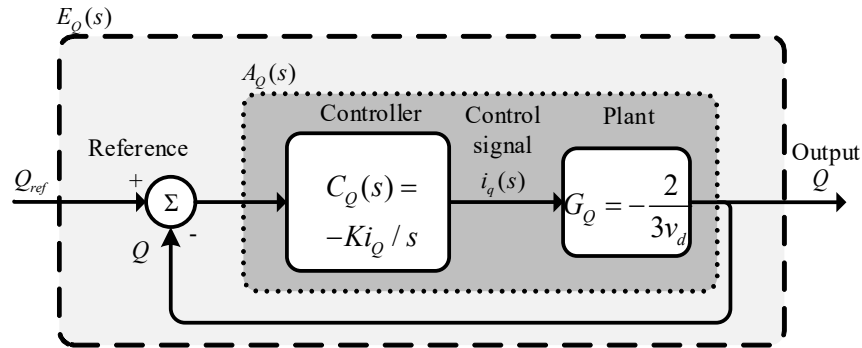


Figure 21: Schematic Diagram of the Reactive Power Control Loop

Figure 22 shows the digital implementation of the reactive power controller.

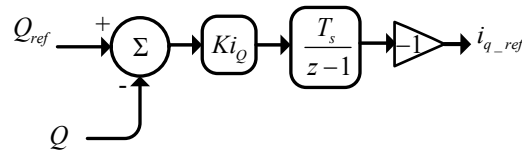


Figure 22: Digital Implementation of the Reactive Power Controller

The step response and bode plots of the reactive power closed loop control system for a bandwidth of  $\alpha_p = 220$  rad. ( $t_{r\_p} = 0.01$  sec) is similar to the one presented in Figure 20.

## 2.6. Introduction to IMC Controllers

The internal model control (IMC) technique relies on the “internal model” principle whose philosophy states that a control action over a plant can be achieved only if the control system includes, either implicitly or explicitly, some representation of the process to be controlled [9, 10]. Figure 23 shows the structure of the IMC.

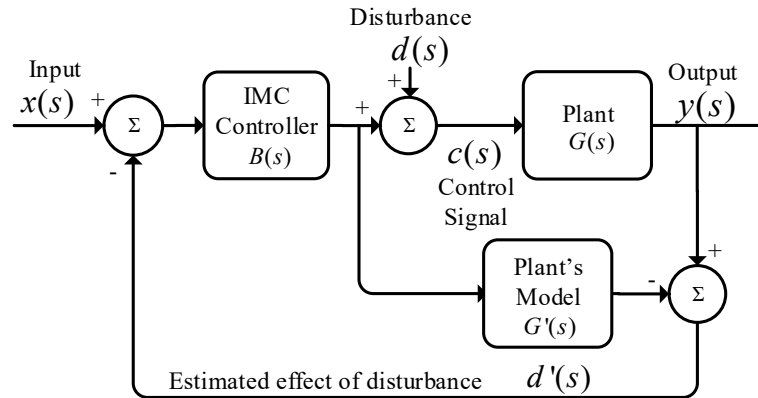


Figure 23: IMC Controller Structure.

As seen in Figure 23, the model of the plant to be controlled ( $G'(s)$ ) is to be an exact representation of the plant itself ( $G(s)$ ) and considering that no disturbance is present, then the estimated effect of disturbance  $d'(s)$ , resulting from the difference between the plant output and the plant model output, turns zero and the close loop system turns equal to the open loop system. On this condition, an IMC controller of the type  $B(s) = G^{-1}(s)$  implies a perfect theoretical control then. However, such ideal control cannot be implemented by two main reasons,

- a) The need of use pure differentiators, (in case the model of the plant is proper)
- b) Infinitely large excursions of the manipulative variable for infinitely small high frequency disturbances (which cannot be implemented realistically in any digital or analog controller).

For a realizable control, the IMC structure introduces a low pass filter  $L(s)$  in cascade to the IMC controller. The filter is designed to add poles to  $G(s)$  in order to turn the controller transfer function proper. The filter  $L(s)$  is usually of the type

$$L(s) = \left( \frac{\alpha}{s + \alpha} \right)^n \quad (18)$$

Where the order of the filter,  $n$ , is chosen accordingly to the order of  $G(s)$ , and  $\alpha$  is regarded as the closed loop bandwidth of the filter, for a first order filter.

The IMC controller has the advantage of having the controller parameters related in a unique, straightforward manner to the model parameters with  $\alpha$  being the only controller variable to be adjusted.

[The need of an additional degree of freedom for poorly damped processes.](#)

When there is a set-point change in a closed loop control system, the mathematical inertia of the controller combines with the physical inertia of the process; this combination damps the process's response to a set-point change. However, if an unexpected load ever disturbs the process abruptly, a set point tracking controller will tend to overreact and cause the process variable to oscillate unnecessarily. This is because a set point tracking controller

does not play a significant role in determining how the process reacts to a disturbance, as such, the load disturbance rejection of the closed loop system, even with the use of a fast IMC or PID controller, is still determined by the process (see Figure 24).

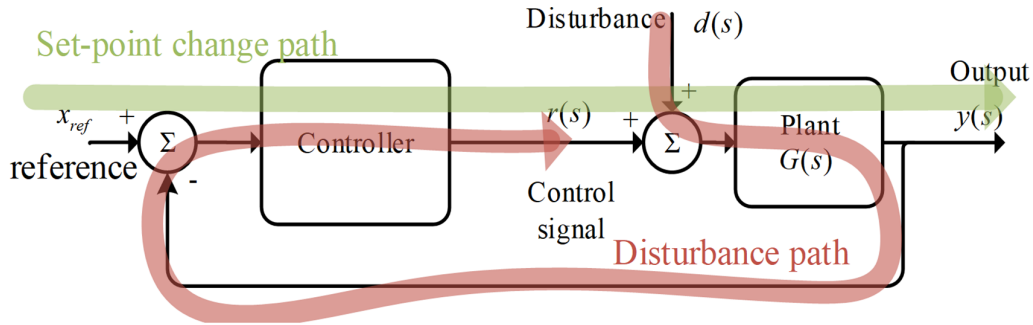


Figure 24 Set-point and Disturbance Paths in a Closed Loop Controller

To further improve the performance of the IMC controller, an inner feedback loop to  $R$  can be added to provide an additional degree of control freedom to speed up the load disturbance rejection a poorly damped plant. This additional control loop is used to speed up the natural response of the plant by moving the pole of the plant away from the origin within the negative side of the real axis. The configuration of the additional control loop is shown in Figure 25.

By adding a feedback loop the transfer function of the improved plant  $M_{dc}(s)$  turns to be

$$M(s) = \frac{G(s)}{1 + G(s)R} = \frac{1}{G^{-1}(s) + R} \quad (19)$$

where  $M(s)$  is the new transfer function of the plant augmented with an inner feedback loop gain  $R$ .

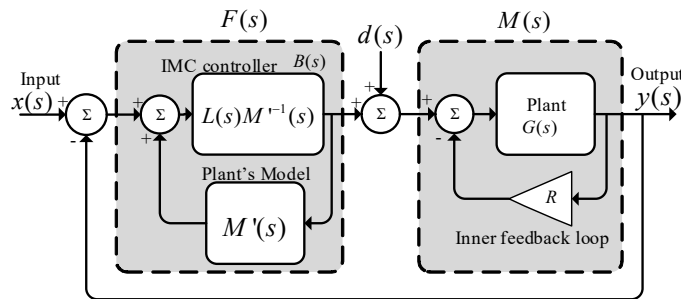


Figure 25: The Two Degrees of Freedom IMC Configured as a PI Controller

This IMC with two degrees of freedom is especially useful for the poorly damped systems of the inverter such as the dc circuit (see section 2.8).

The processes to be controlled using the two degrees of freedom IMC controller are the  $dq$  currents and the DC voltage. The transfer functions of these processes are given by a first order transfer function, implying a first-degree filter for their respective IMC controller. Under this consideration the transfer function of the IMC control  $F(s)$  (considering that  $M'(s)$  is the model of  $M(s)$ ) is shown in equation (20).

$$F(s) = \frac{B(s)}{1 - B(s)M'(s)} = \frac{L(s)M^{r-1}(s)}{1 - L(s)M^{r-1}(s)M'(s)} = \frac{\alpha}{s} M^{r-1}(s) \quad (20)$$

The additional degree of freedom is chosen, in each case controller case, to make the process dynamics as fast as the controller dynamics. This allows the load disturbance rejection to be as fast as the controllers closed loop dynamics. To achieve this, the pole  $R$  is set in the inner feedback loop to match the pole of the IMC controller in the transfer function from the disturbance  $d(s)$  to output signal of the plant  $y(s)$ , which is:

$$\frac{y(s)}{d(s)} = \frac{M(s)}{1 + F(s)M(s)} = \frac{M(s)}{1 + (\alpha/s)M^{r-1}(s)M(s)} = \left( \frac{s}{s + \alpha} \right) \frac{1}{G^{-1}(s) + R} \quad (21)$$

If  $R$  is chosen appropriately, equation (21) can be reduced to

$$\frac{y(s)}{d(s)} = \left[ \left( \frac{s}{s + \alpha} \right) \frac{K}{s + \alpha} \right] = K \left[ \frac{s}{(s + \alpha)^2} \right] \quad (22)$$

where  $K$  is a constant.

As can be noticed in equation (22), the load disturbance  $d(s)$  is damped with the same time constant as the closed loop control.

The IMC controller closed loop bandwidth  $\alpha$  is chosen accordingly the rise time  $t_r$  needed for the output signal  $y(s)$ , which for a first order can be selected using equation (13).

To illustrate the advantages of using the 2 degrees of freedom IMC, Figure 26 shows a simulation result where a first order plant is controlled by a PI using technical optimum (pole-zero matching) and the same plant is controlled using an IMC controller. Both controllers are exposed at a set-point change at  $t=0.1$  and then to a disturbance at  $t=0.2$ . As seen in Figure 26 both the PI controller and the IMC controller respond with the same dynamics for a set point change, however a much better transient response (in terms of overshoot and settling time) is provided by the 2 degrees of freedom IMC during a disturbance.

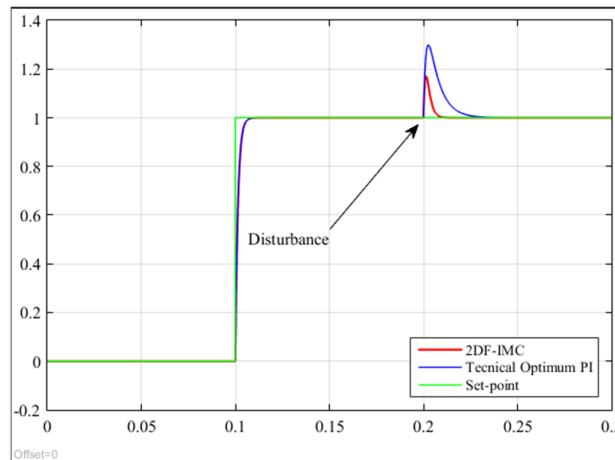


Figure 26: IMC and PI Controller Transient Response Comparison for a First Order Plant

## 2.7. $d$ and $q$ Current Control

The equations defining the behaviour of the currents between any of the VSC of the B2B converters and their respective ac grids expressed in  $dq$  components are

$$\begin{aligned} v_{d\_inv} &= ri_d + L \frac{d}{dt} i_d - \omega_s Li_q - v_d \\ v_{q\_inv} &= ri_q + L \frac{d}{dt} i_q + \omega_s Li_d - v_q \end{aligned} \quad (23)$$

where  $r$  and  $L$  are, respectively, the equivalent resistance and inductance between the VSC and the grid,  $v_{d\_inv}$  and  $v_{q\_inv}$  are the  $dq$  components of the average voltages generated by the VSC.

The transfer functions used to control the  $dq$  inverter currents can be reduced to a similar expression if the cross-coupling terms ( $\omega_s Li_q$  and  $\omega_s Li_d$ ), and the grid voltage components, ( $v_d$  and  $v_q$ ) from equation (23) are considered disturbances, not present during the calculation of the  $dq$  current control, instead being numerically compensated as shown in section 2.9. Hence, the VSCs current-to-voltage relationships in the  $dq$  frame are:

$$\frac{i_d(s)}{v_{d\_inv}(s)} = \frac{i_q(s)}{v_{q\_inv}(s)} = \frac{i(s)}{v_{inv}(s)} = G_i(s) = \frac{1}{Ls + r} \quad (24)$$

If an inner feedback loop of gain  $R_i$  is added to the inverter current plant to add active damping to  $G_i$  (i.e a second degree of freedom as shown in equation (19)) a transfer function of the following type is obtained:

$$M_i(s) = \frac{1}{R_i + Ls + r} \quad (25)$$

The inner feedback loop is implemented to the plant by means of making the input signal to the plant equal to

$$v_{inv}(s) = v_{inv}'(s) - i(s)R_i$$

where  $v'(s)$  is the output of the IMC current controller  $F_i(s)$ , which, accordingly to equation (20) turns to be

$$F_i(s) = \alpha_i L + \frac{(r + R_i)\alpha_i}{s} \quad (26)$$

where  $\alpha_i$  is the bandwidth of the closed loop system of  $dq$  current control system.

from (26) we can deduce the controller constants as

$$\begin{aligned} Kp_i &= \alpha_i L \\ Ki_i &= (r + R_i)\alpha_i \end{aligned} \quad (27)$$

Now, we can select  $R_i$  to match the pole of  $M_i(s)$  with the pole of  $F_i(s)$  on the transfer function from the disturbance  $d_i(s)$  to the output of the plant  $i(s)$ , as described in equation (21). Thus, selecting  $R_i$  to have the value of

$$R_i = \alpha_i L - r \quad (28)$$

we can prove that the relationship  $v_{inv}(s) / d_i(s)$  turns to be

$$\frac{v_{inv}(s)}{d_i(s)} = \frac{s}{L(\alpha_i + s)^2} \quad (29)$$

As seen in equation (29), the disturbances coming from  $d_i(s)$  are rejected by the plant and the controller with the same time constant, which in turn depends on  $\alpha_i$ . Figure 27 shows the inverter current control loop.

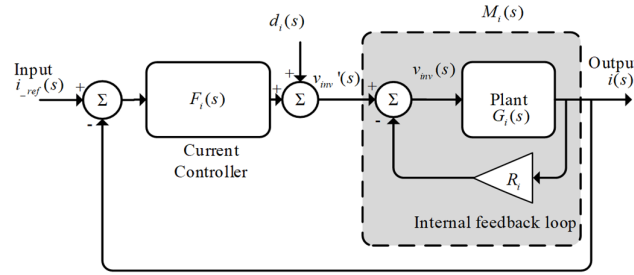


Figure 27: Inverter Currents Control Loop

Figure 28 shows the digital implementation of the IMC current controller

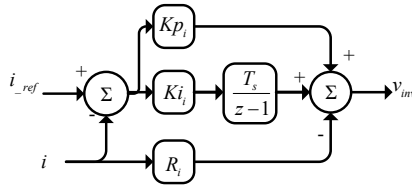


Figure 28: Digital Implementation of IMC Current Controller

## 2.8. Direct Voltage Controller

The DC plant equation of the GSC is defined as:

$$C \frac{dv_{dc}}{dt} = i_{dc\_load} + i_{dc} \quad (30)$$

where  $i_{dc\_load}$  is the dc current absorbed by the load or the DC network connected to dc side of the inverter  $i_{dc}$  is the DC current of the inverter and  $C$  is full equivalent capacitance of the DC circuit. The average value of  $i_{dc}$  can be represented in term of the ac currents and modulator signals. In  $dq$  reference frame this is:

$$i_{dc} = \frac{3}{4}(m_{d\_inv}i_d + m_{q\_inv}i_q) \quad (31)$$

where  $m_{d\_inv}$  and  $m_{q\_inv}$  are the  $d$  and  $q$  components of the inverter modulator signal. The equation of the ac circuit of the GSC, in terms of modulator signals is thus given by [11]:

$$\left. \begin{aligned} \frac{v_{dc}}{2}m_d = v_{d\_inv} &= ri_d + L\frac{di_d}{dt} - L\omega i_q - v_d \\ \frac{v_{dc}}{2}m_q = v_{q\_inv} &= ri_q + L\frac{di_q}{dt} + L\omega i_d - v_q \end{aligned} \right\} \quad (32)$$

Substituting equation (31) and equation (32) in equation (30) and assuming the grid voltage is aligned to  $v_d$  (i.e.  $v_q = 0$ ) the following expressions for  $i_{dc}$  and the inverter dc power  $P_{dc}$  are obtained:

$$i_{dc} = \frac{3R}{2v_{dc}}(i_d^2 + i_q^2) + \frac{3L}{2v_{dc}}\left(i_d\frac{di_d}{dt} + i_q\frac{di_q}{dt}\right) - \frac{3}{2v_{dc}}(v_d i_d) \quad (33)$$

$$i_{dc}v_{dc} = P_{dc} = \frac{3R}{2}(i_d^2 + i_q^2) + \frac{3L}{4}\frac{d}{dt}(i_d^2 + i_q^2) - \frac{3}{2}(v_d i_d) \quad (34)$$

Equation (34) shows that the dc side power of the inverter is composed by the sum of the resistive losses in the ac side ( $3(i_d^2 + i_q^2)R/2$ ) plus the energy stored in the inductance between the GSC and the AC grid ( $\frac{3L}{4}\frac{d}{dt}(i_d^2 + i_q^2)$ ) plus the AC active power ( $\frac{3}{2}(v_d i_d)$ ).

Since the resistive losses are very small, they can be neglected from the dynamic equation of  $P_{dc}$ , also for low values of  $L$  the energy stored in the inductance can be neglected too. Thus, the equation describing the dynamics of the DC voltage can be simplified as:

$$\begin{aligned} C v_{dc} \frac{dv_{dc}}{dt} &= v_{dc}(i_{dc\_load} + i_{dc}) \rightarrow \\ C v_{dc} \frac{dv_{dc}}{dt} &= P_{load} + P_{dc} \rightarrow \\ \frac{C}{2} \frac{dv_{dc}^2}{dt} &= P_{load} + \left(-\frac{3}{2}(v_d i_d)\right) \end{aligned} \quad (35)$$

In order to work with linear expressions (assuming  $v_d$  is constant), the output variable of the DC-plant is selected to be the square of the capacitor voltage (i.e. a representation of the energy of the capacitor). Thus, selecting the square of the capacitor voltage to be  $w = v_{dc}^2$  and considering  $P_{load}$  a disturbance, not present during the calculation of the voltage controller, the transfer function of the dc-plant can be presented as:

$$-\frac{w(s)}{i_d(s)} = -G_w(s) = -\frac{3v_d}{Cs} \quad (36)$$

As seen in equation (36)  $-G_w(s)$  has a pole in the origin, which makes it very susceptible to disturbances.

Following the procedure for designing a two degree of freedom IMC controller, an inner feedback loop of gain  $R_w$  is added to the DC-plant to add active damping to  $G_w$  (i.e. a second degree of freedom as shown in equation (19)). This is:

$$-M_w(s) = -\frac{G_w(s)}{1 + G_w(s)R_w} = -\frac{3v_d}{Cs + 3v_d R_w} \quad (37)$$

The inner feedback loop is implemented to the DC-plant by means of making the input signal to the dc-plant equal to

$$i_d(s) = i_d'(s) - w(s)R_w \quad (38)$$

where  $i_d'(s)$  is the output of the IMC current controller  $F_w(s)$ , which, accordingly to equation (20) turns to be

$$F_w(s) = \frac{\alpha_w}{s} (-)M_w^{-1}(s) = \frac{\alpha_w}{s} \left( -\frac{3v_d}{Cs + 3v_d R_w} \right)^{-1} = -\left( \frac{\alpha_w C}{3v_d} + \frac{\alpha_w R_w}{s} \right) \quad (39)$$

where  $\alpha_w$  is the bandwidth of the closed loop system of the  $v_{dc}^2 = w$  control system.

From equation (39) the controller constants can be calculated as:

$$\begin{aligned} Kp_w &= \frac{\alpha_w C}{3v_d} \\ Ki_w &= \alpha_w R_w \end{aligned} \quad (40)$$

Now,  $R_w$  can be selected to match the pole of  $M_w(s)$  with the pole of  $F_w(s)$  on the transfer function from the disturbance  $d_w(s)$  (in this case  $P_{load}$ ) to the output of the plant  $w(s)$ . The process to do this is presented in equation (21). Thus, selecting  $R_{dc}$  to have the value of

$$R_{dc} = \frac{1}{3} \frac{\alpha_{dc} C}{v_d} \quad (41)$$

it can be shown that the relationship  $v_{dc}^2 / P_{load}$  turns to

$$\left( \frac{v_{dc}^2(s)}{P_{load}} \right) = \left( \frac{2s}{(Cs + 3v_d R_{dc})(s + \alpha_{dc})} \right) = \left( \frac{2s}{C(s + \alpha_{dc})^2} \right) \quad (42)$$

As seen in equation (42), a power step of magnitude  $|P_{load}|$  is rejected by the dc plant with the same time constant of closed loop controller, which in turn depends on  $\alpha_w$ . Figure 29 shows the DC voltage control loop.

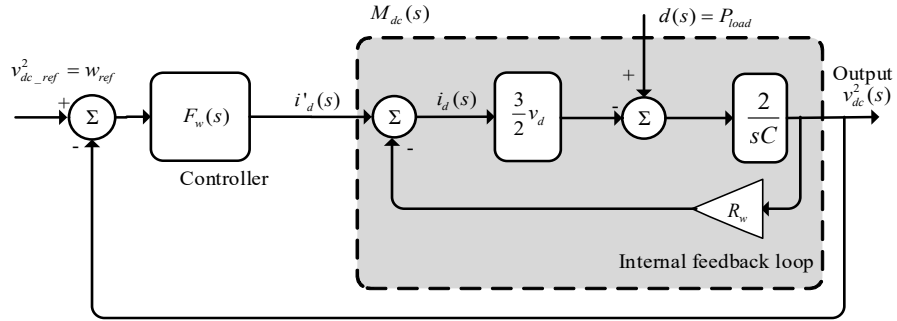


Figure 29: DC Voltage Control Loop

Figure 30 shows the digital implementation of the IMC controller

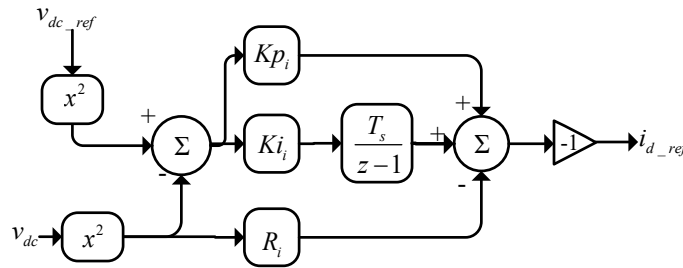


Figure 30: Digital Implementation of DC Voltage Controller

## 2.9. Cross Coupling Term Elimination

The cross coupling elimination allows the independent control of the  $d$  and  $q$  currents by eliminating the terms that link the two currents in the equations of the voltage of the VSCs. In order to do this, the following terms are added to the voltage control signals of the VSCs

For the  $d$  voltage control signal the term  $v_d - \omega_s L i_q$  is added, where  $\omega_s = 2\pi \cdot 50$

For the  $q$  voltage control signal the term  $v_q + \omega_s L i_d$  is added

Using this additions, the equation of the voltages of the inverter presented in equation (23) are changed to

$$\begin{aligned}
 v'_{d\_inv} + (v_d - \omega_s L i_q) &= r i_d + L \frac{d}{dt} i_d - \omega_s L i_q - v_d \\
 v'_{q\_inv} + (v_q + \omega_s L i_d) &= r i_q + L \frac{d}{dt} i_q + \omega_s L i_d - v_q \\
 &= \\
 v_{d\_inv} &= r i_d + L \frac{d}{dt} i_d \\
 v_{q\_inv} &= r i_q + L \frac{d}{dt} i_q
 \end{aligned} \tag{43}$$

Figure 31 shows the digital implementation of the cross coupling term elimination

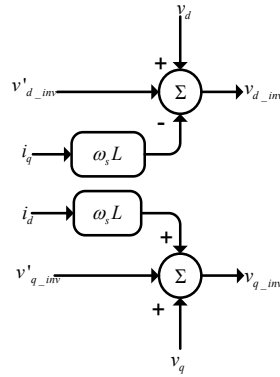


Figure 31: Digital Implementation of the Cross Coupling Term Elimination

## 2.10. Conversion to Modulator Signals

The conversion to modulator signal stages converts the  $d$  and  $q$  voltage command signal from the controllers to equivalent  $d$  and  $q$  modulator signals. This conversion stage also enforces an optimal limitation of the  $d$  and  $q$  modulator signals in case the magnitude of the voltage command signals surpasses the voltage capacity of the VSC, which is limited to a maximum of half the voltage in the DC link.

The optimal limitation of the control voltages is carried out in several stages:

First, a detection stage monitors the command voltage signals from the controllers and activates a flag in case the following inequality is true for sinusoidal pulse width modulation (SPWM)

$$|v_{mag}| > \frac{v_{dc}}{2} \quad (44)$$

Where  $v_{mag} = \sqrt{v_{d\_inv}^2 + v_{q\_inv}^2}$  is the magnitude of voltage that the inverter is commanded to generate. If  $|v_{mag}|$  turns larger than the maximum voltage that the VSC can generate, a limitation scheme follows next.

The limitation scheme makes use of the “circular method” to limit the voltage command signal [12, 13]. Here, the polar quantities of the  $d$  and  $q$  command voltages (i.e. the magnitude and angle) are calculated and the magnitude of the saturated voltage command signal is reduced to fit within a circle of radius  $v_{dc}/2$  while keeping the same angle  $\angle v_{mag}$  of the original  $dq$  command voltage. Figure 32 shows the geometric interpretation of the circular method for SPWM.

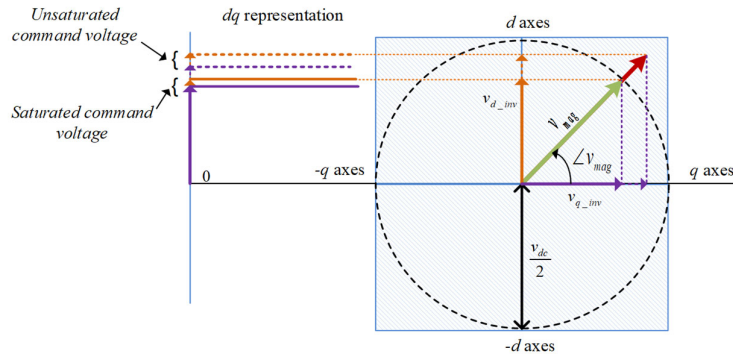


Figure 32: Circular Method Limitation of the  $d$  and  $q$  Control Voltage Signals

This circular method saturation produces a coherent reduction of the  $dq$  voltage command signals without prioritizing one voltage command over the other. Thanks to this the cross coupling elimination and disturbance rejection of the controller scheme is used at its maximum capacity. If there is the need to prioritize the use of a current over the other one, such task can be carried out in the controllers commanding the  $dq$  current loops.

Finally the saturated  $dq$  command signals are divided by  $v_{dc} / 2$  to turn them into the modulator signals  $m_{d\_inv}$  and  $m_{q\_inv}$ . Finally, the modulator signals are sent to the  $dq$  to  $abc$  transformation. The schematic representation of the saturation and modulator conversion system is presented in Figure 33.

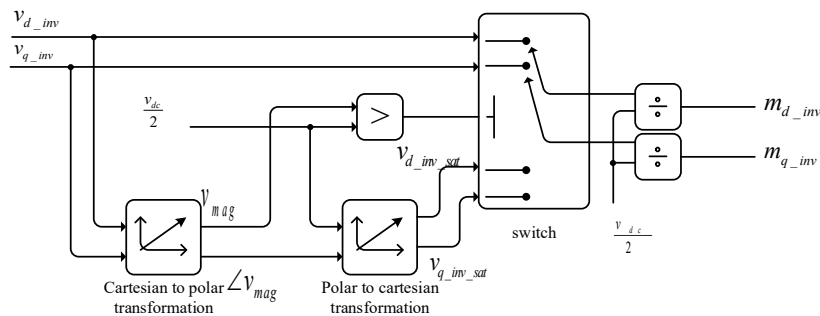


Figure 33: Diagram of the Voltage Saturation and Conversion to Modulator Signal

### 2.11. dq0 to abc Transformation

The  $dq0$  to  $abc$  transformation changes the dc representation of the VSCs modulators  $m_{d\_inv}$  and  $m_{q\_inv}$  to the three phase  $abc$  modulator signals  $m_{a\_inv}$ ,  $m_{b\_inv}$  and  $m_{c\_inv}$ . The transformation is applied as follows

$$\begin{bmatrix} m_{a\_inv} \\ m_{b\_inv} \\ m_{c\_inv} \end{bmatrix} = \frac{2}{3} \begin{bmatrix} \sin \theta_{dq} & \cos(\theta_{dq}) & 1 \\ \sin\left(\theta_{dq} - \frac{2\pi}{3}\right) & \cos\left(\theta_{dq} - \frac{2\pi}{3}\right) & 1 \\ \sin\left(\theta_{dq} + \frac{2\pi}{3}\right) & \cos\left(\theta_{dq} + \frac{2\pi}{3}\right) & 1 \end{bmatrix} \begin{bmatrix} m_{d\_inv} \\ m_{q\_inv} \\ m_{0\_inv} \end{bmatrix} \quad (45)$$

### 2.12. Simulink Implementation of the Back to Back converter

Figure 34 shows the Simulink implementation of the GSC along with its main controllers and its user interface. As seen in the figure, the Simulink model consists of a 2 Level VSC interconnected to the grid via a LR filter. The VSC works in average model of operation, meaning the voltages at its terminals are not produced by the switching of power electronics, rather they are a multiplication of the modulator signals with the DC voltage. By using average mode of operation of the VSC, the simulation can be carried out using sampling times of 50-100 micro seconds, which are suitable to analyse power system phenomena. The average simulation of a VSC reproduces faithfully the fundamental frequency dynamics of a VSC without the need of smaller sampling times to include the switching of the power electronic devices. Since the developed AC networks has the purpose of studying electromagnetic and electromechanic transients, but not high frequency harmonics product of power electronic switching, the average simulation of the VSCs is considered enough for the simulation needs of this project.

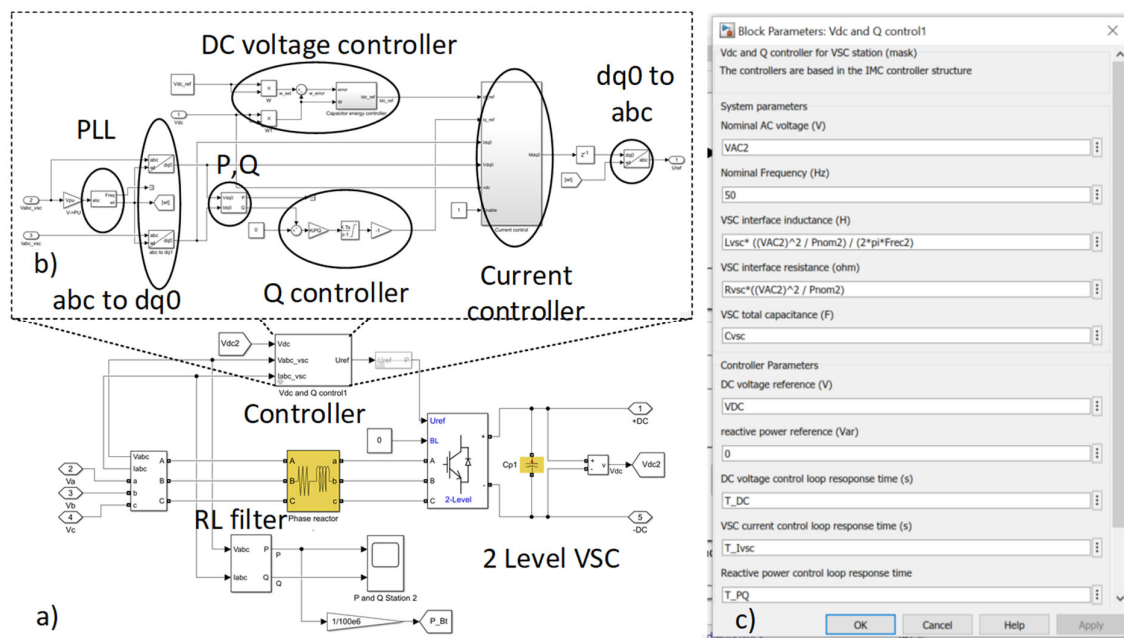


Figure 34: Simulink implementation of the GSC. a) Simulink Model, b) Controller structure, c) controller user interface

Figure 34 b) shows the internal structure of the GSC controller, this structure follows the layout presented in Figure 15. Figure 34 c) shows the user interface of the GSC controller. This user interface requests from the user parameters of nominal voltage and frequency of the grid, as well as the value of in inductance and resistance of the RL filter and the value in

capacitance of the DC circuit. Latter on the interface requests the references for the DC voltage and reactive power controllers. Finally, the response time of the control closed loops of the DC voltage, reactive power and GSC currents is requested. The response time selection allows the user to define how fast the closed loop controller will track a set point change. For example, a response time of 0.01ms for the DC voltage loop implies that the gains of the controllers are adjusted to deliver a control action that will change the DC voltage from a previous reference into a new reference in 0.01 ms (more specifically the response time defines the “rise time” required by the response to rise from 10% to 90% of its final value) Since the controllers are of the IMC type, it is only required to specify the response time of the close loop control to calculate the bandwidth of the controller and the proportional, integral, and active damping gains if the IMC controller. All these calculations are carried out automatically by the controller for each closed loop control.

Figure 35 shows the Simulink representation of the MSC with its main controllers and its user interface.

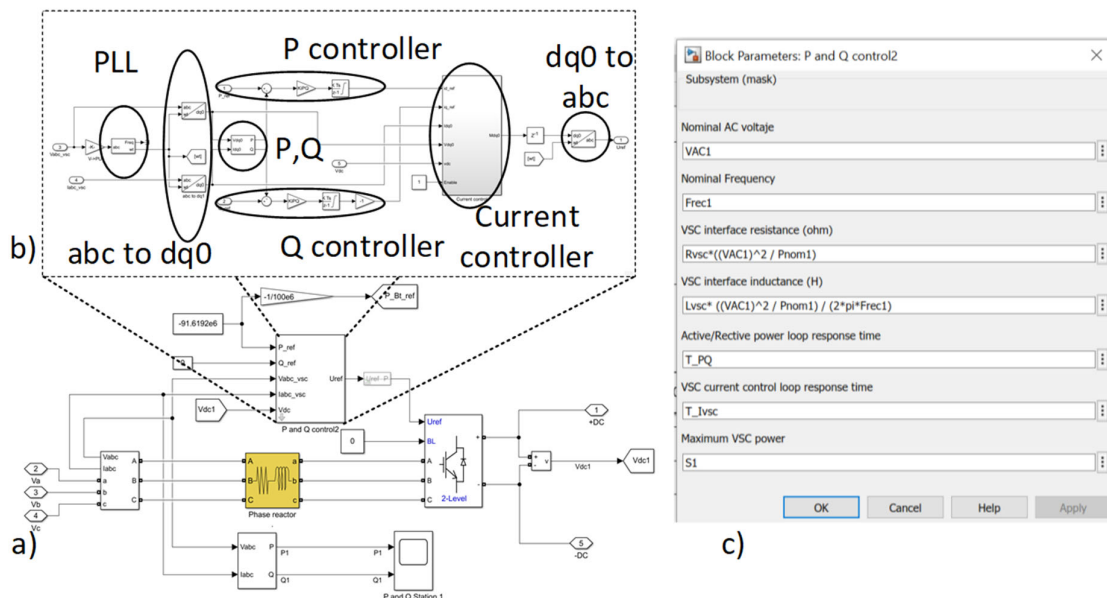


Figure 35: Simulink implementation of the MSC, a) Simulink Model, b) Controller structure, c) controller user interface

Just as in the case of the GSC the MSC consists of a 2-Level 3-phase VSC working in average mode of operation. The MSC is interfaced to the machine using a RL filter. In the future, a more accurate representation of the internal resistance and impedance of the hydro generator could allow to use these values as the RL filter required for the proper functioning of the VSC. The controller of the MSC modifies the active and reactive power interchange at the terminals of the GSC, in future developments, these controllers will be upgraded to control other characteristics of the flexible hydro generator such as its electrical torque and speed. The detail of the internal controllers of the MSC can be seen in Figure 35 b). Figure 35 c) shows the user interface of the MSC controllers where the values of the AC voltage, Frequency as well as the inductance and resistance of the RL filter are provided. The user then defines the response time of the active and reactive power loops as well as the response time of the current loops.

The current controller module is the same for the GSC and MSC. The current control module implements the IMC current control as well as cross coupling term elimination and conversion to modulator signals. Figure 36 show the Simulink implementation of the current control module. As seen in the figure, the current control structure follows the layout defined in Figure 15.

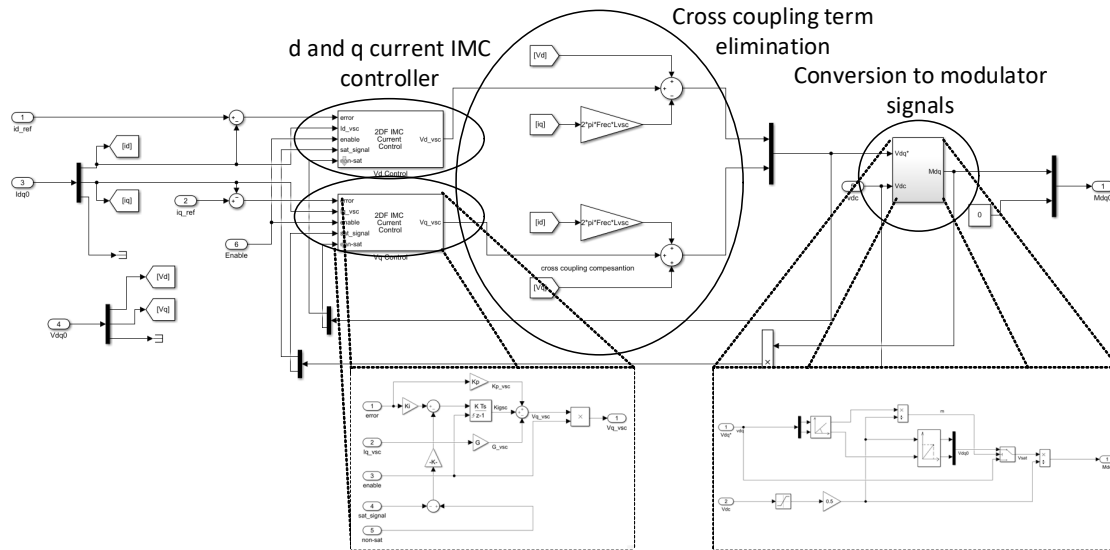


Figure 36: Current controller of the GSC and MSC

### 2.13. Steady state simulation of the B2B converter controllers

To test the performance of the B2B controllers, the active power reference of the MSC is changed in a step manner from 0 to 90MW at  $t=2$  seconds, and from -90MW to 50MW at  $t=2.2$  seconds. To enable the sustained provision of the requested power by the MSC, the MSC is connected to an ideal AC source. A change in the power reference of the MSC will trigger a change in the d current reference of the MSC. The rise time of the active power control loop is 10ms whereas the rise time of the current loops in the MSC and GSC is 2ms. The requested power by the GSC will be injected/absorbed to/from the DC link changing the DC voltage value. On the detection of a change of DC voltage, the DC voltage controller of the GSC will absorb/inject energy to the DC capacitor to keep the DC voltage close the reference value. The reference DC voltage for the GSC is 50kV, the closed loop rise time of the DC voltage controller is 6ms. To evaluate the coordinated control action of the MSC and GSC converters Figure 37 shows the control variables of each VSC.

As seen in Figure 37 a), the Active power reference is followed closely by the real active power production of the MSC, the rise time of the active power signal is consistent with the selected rise time for the controller. The change in active power reference commands a change in the  $i_d$  current reference as seen in Figure 37 c). The  $i_d$  current reference is followed closely by the real  $i_d$  current with a rise time of 2ms. Figure 37 d) shows the behaviour of the reactive power of the MSC which it is commanded to be 0 throughout the simulation period. As seen in Figure 37 d), the reactive power of the GSC follows the reference in steady state. During changes of active power, the value of  $i_q$  current is changed because of the cross coupling

term linking  $i_d$  and  $i_q$  currents. This is reflected as a small transient change in reactive power which is quickly compensated by the reactive power controller. The transient change in  $i_q$  currents can also be seen in Figure 37 d). The sudden injection of active power into the DC bus produces an increase in the DC voltage of the B2B, however this voltage increase is quickly controlled by the DC voltage controller of the GSC as seen in Figure 37 f). In order to control the DC voltage the GSC commands the  $i_d$  current to inject power into the AC grid, as such the  $i_d$  current of the GSC increases to a value of 4000 amperes as seen in Figure 37 g). Just as in the case of the MSC, the GSC converter  $q$  current is affected by the cross coupling terms, however the reactive power controller of the GSC manages to bring back the value of  $i_q$  current to 0 following its response time characteristics.

At  $t=2.2s$ , a change in the polarity of active power reference in the MSC is triggered, changing the active power provision from  $-90MW$  to  $50MW$  as seen in Figure 37 a). This sudden change of power flow, produces a transient reduction in the DC bus voltage, however this is quickly compensated by DC voltage controller in the GSC which commands a change in its  $i_d$  current reference to around  $-2000$  amperes as seen in Figure 37 g).

The smooth response of the controllers following a set point change shows the good design of the controller scheme. The fast and oscillation free control of the DC voltage shows the advantages of using the 2DF-IMC structure.

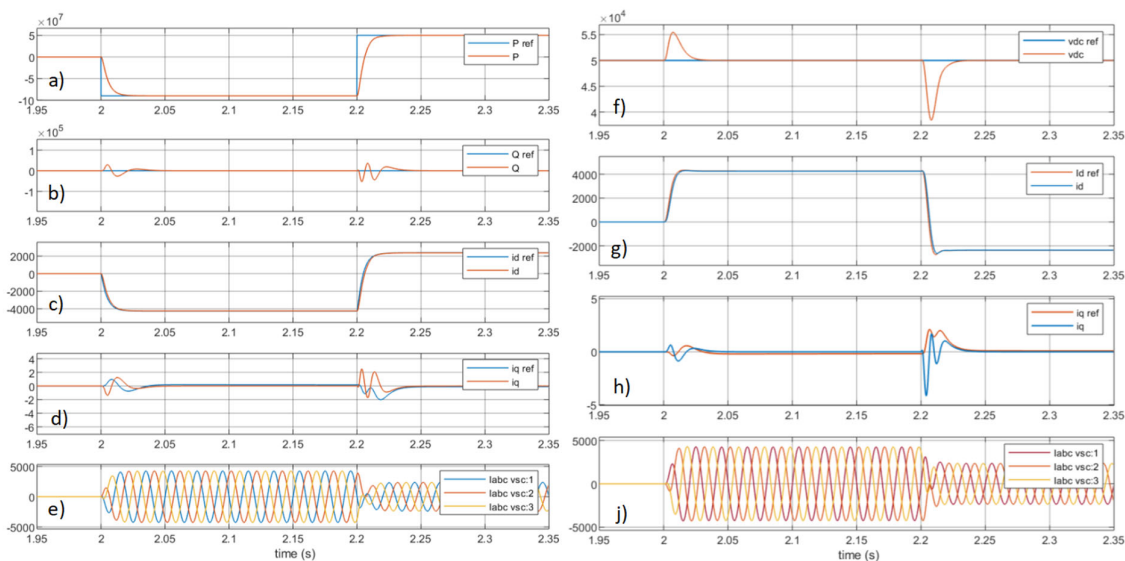


Figure 37: B2B control variables during an active power reference change. a) MSC Active power b) MSC reactive power c) MSC  $i_d$  current d) MSC  $i_q$  current e) MSC abc currents, f) GSC DC voltage g) GSC  $i_d$  current h) GSC  $i_q$  current, j) GSC abc currents.

A second test of controller performance is presented in Figure 38. In this case, the GSC is commanded to change the DC voltage level of the DC bus from  $50kV$  to  $60kV$  at  $t=2s$  and from  $60kV$  to  $40kV$  at  $t=2.2s$ . In the meantime, the MSC is commanded to provide a steady active power provision of  $50MW$  into the DC bus.

As seen in Figure 38 f), the DC voltage reference changes from  $50kV$  to  $60kV$  at  $t=2s$ , the response of the DC voltage to the controller is a smooth transition to the new set point value

with a rise time of 6ms, just as indicated by the controller. The change of DC voltage affects minimally the control variables of the MSC as seen in Figure 38 a) to e). This shows the advantages of using active damping to reject external disturbances. Figure 38 g) shows the d current of the GSC. In order to increase the voltage of the DC bus, the GSC has to allow some of the power flowing in the DC bus to charge the DC capacitor rather than delivering it to the AC grid. Because of this, during the DC capacitor charging period, the d current flow to the AC grid decreases from around 2000 Amps to almost 0 Amps. After the DC voltage of the capacitor reaches its new steady state value, the power provision from the MSC is delivered fully to the AC grid as seen in Figure 38 g). At t=2.2s the DC voltage is commanded to change from 60kV to 40kV, this implies discharging the DC capacitor. As seen in Figure 38 f), the discharge of the capacitor is done in the same smooth manner as in the charging command. In order to discharge the capacitor, the GSC increases the amount of  $i_d$  current injected to the AC grid to about 4000 Amps for a short period of time.

The two simulations presented in Figure 37 and Figure 38 show the capability of each individual controller to provide accurate set point tracking and enhanced disturbance rejection. This is characteristics are highly desirable for the B2B converter when subjected to the dynamic conditions of the AC grid.

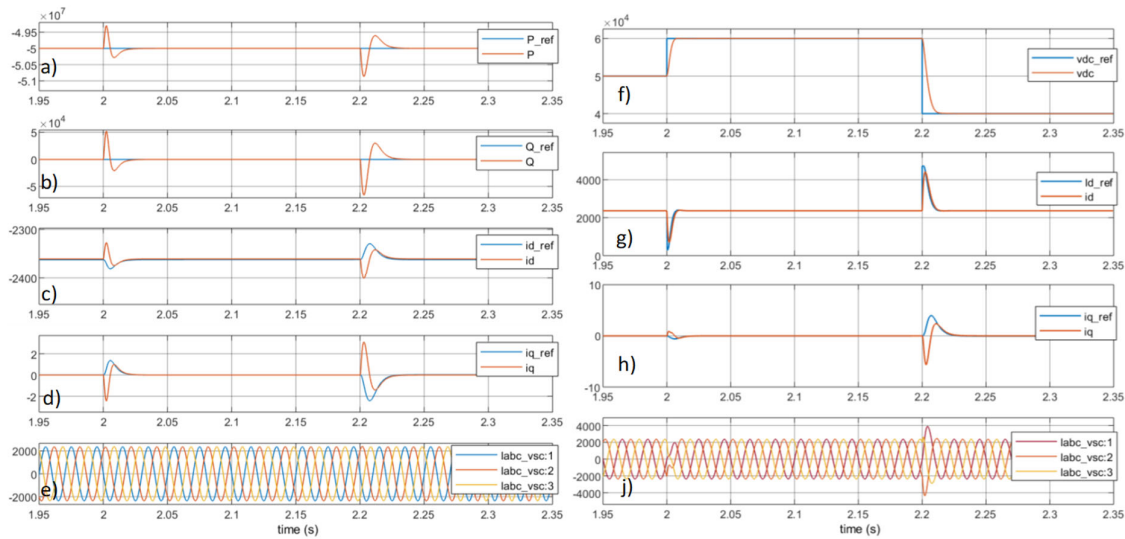


Figure 38: B2B control variables during DC voltage reference change. a) MSC Active power b) MSC reactive power c) MSC  $i_d$  current d) MSC  $i_q$  current e) MSC abc currents, f) GSC DC voltage g) GSC  $i_d$  current h) GSC  $i_q$  current, j) GSC abc currents.

### 3. Dynamic Simulation of the full AC grid

This section evaluates the behaviour of the B2B converter subjected to the dynamic AC grid situations generated by the generated simulation model. This section will test the stability of the B2B controllers with the purpose to provide controller designers with a robust framework where more advance controllers for the B2B can be implemented for the provision of ancillary services to the AC grid and for fault-ride-through compliance.

#### 3.1. Simulation of Frequency Excursions

The first full simulation test is designed to subject the B2B converter to a frequency excursion with moderate power oscillations. This is the study case presented in Figure 8 a) to e). Figure 39 shows the angular frequency of all the machines of the system during a loss of generation scenario and compares it with the frequency measured by the PLL of the GSC. If the PLL of the GSC is able to follow the frequency changes, then this will mean the converter will remain synchronized to the power grid during the frequency excursion.

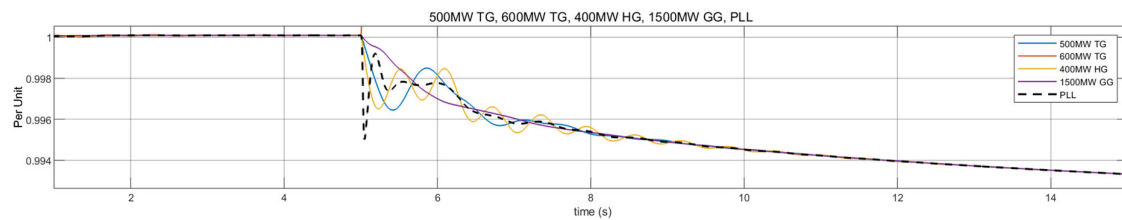


Figure 39: Angular frequency of Machines and PLL behaviour during an event of loss of generation with moderate power oscillations

As seen in Figure 39, the PLL is able to synchronize correctly with the AC grid. This enables the B2B the continuous delivery of its power output during the frequency excursion. To evidence this, Figure 40 shows the control variables of the GSC during the frequency excursion event.

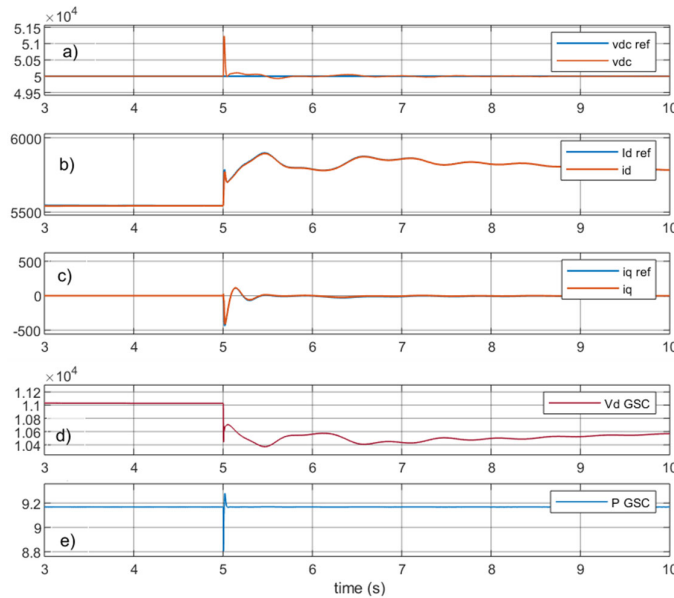


Figure 40: GSC behaviour during an event of loss of generation with moderate power oscillations, a) DC voltage, b)  $i_d$  current, c)  $i_q$  current, d)  $v_d$  of AC grid e) Active power of the GSC

As seen in Figure 40 a), the disruption to the DC voltage and currents is minimal during the frequency excursion and the inverter continues its delivery of its set point power as seen in Figure 40 e). The frequency disruption causes changes in the amplitude of the AC voltages at the terminals of the inverter, this can be appreciated in Figure 40 d) where the d voltage magnitude seen at the terminals of the inverter (i.e. the magnitude of the peak phase voltage), however the inverter adjusts its current output at all time (see Figure 40 b) to deliver a constant AC power to the grid.

Figure 41 shows the angular frequency behaviour of the machines connected to the AC grid as well as the B2B PLL for loss of generation event with increased power oscillations. This corresponds to the dynamic case presented in Figure 8 f) to g).

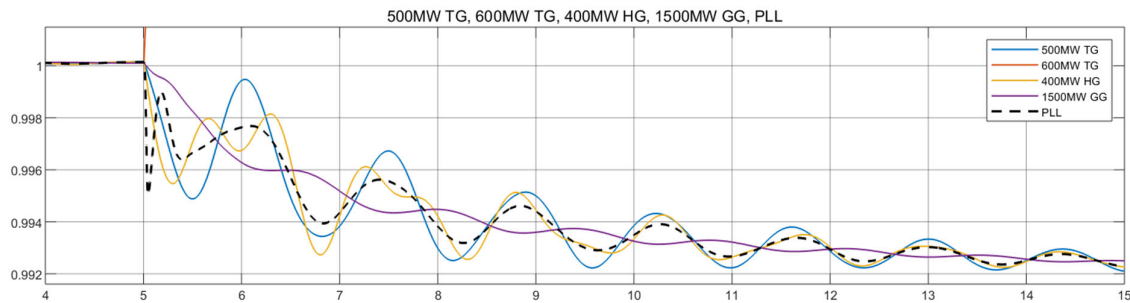


Figure 41: Angular frequency of Machines and PLL behaviour during an event of loss of generation with severe power oscillations

As seen in Figure 41, the PLL is able to synchronize correctly with the AC grid even during times of high frequency oscillations. This enables the B2B the continuous delivery of its power output during the frequency excursion. To evidence this, Figure 42 shows the control variables of the GSC during the frequency excursion event with high power oscillations.

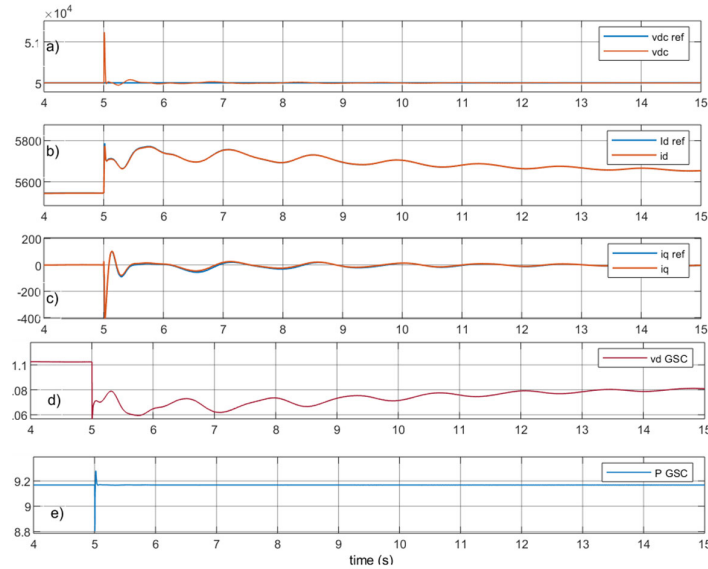


Figure 42: GSC behaviour during an event of loss of generation with severe power oscillations, a) DC voltage, b)  $i_d$  current, c)  $i_q$  current, d)  $v_d$  of AC grid e) Active power of the GSC

As seen in Figure 42 a), the disruption to the DC voltage and currents is minimal during the frequency excursion and the inverter continues its delivery of its set point power as seen in Figure 42 e). The frequency disruption causes changes in the amplitude of the AC voltages at the terminals of the inverter, this can be appreciated in Figure 42 d) where the  $v_d$  voltage magnitude seen at the terminals of the inverter (i.e. the magnitude of the peak phase voltage), however the inverter adjusts its current output at all time (see Figure 42 b) to deliver a constant AC power to the grid.

### 3.2. Faults

Figure 43 shows the behaviour of the B2B converter during the three phase short circuit scenario described in section 1.3.4.

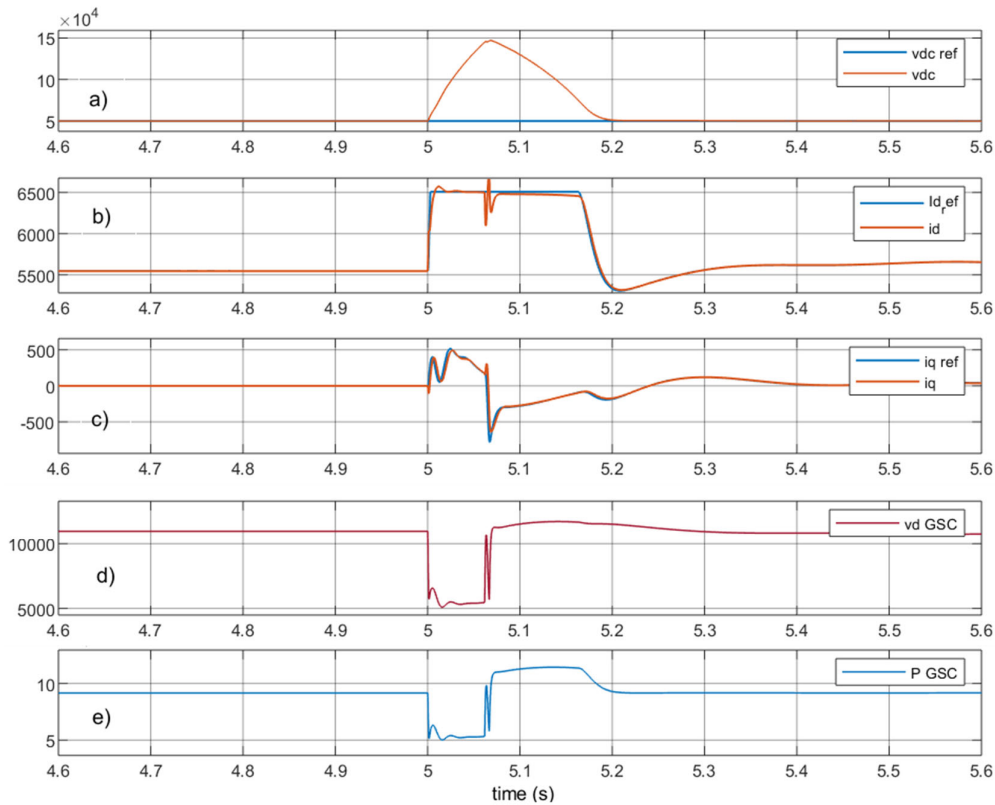


Figure 43: GSC behaviour during an event of a 3 phase fault at AC grid, a) DC voltage, b)  $i_d$  current, c)  $i_q$  current, d)  $v_d$  of AC grid e) Active power of the GSC

By analysing Figure 43 a) in detail, it is evident that the 3 phase fault created a potentially destructive condition for the B2B converter, since the DC voltage reaches values of 150kV (3 times the nominal DC voltage value) during the fault. This would imply the physical destruction of the DC capacitor, since the maximum allowed over voltage for these devices is of around 1.3 PU. The DC overvoltage is not the product of a loss of stability from the GSC controllers, rather, the fault condition severely limited the power export capabilities of the B2B as seen in Figure 43 e). In an attempt to deliver as much active power as possible during the fault period, the GSC increases its d current output up to the maximum current rating of the converter as seen in Figure 43 b), this effort however is not enough to avoid an overvoltage in the DC link. After the fault is cleared and the AC voltage restores to its pre-fault condition the GSC is able to discharge the DC capacitor and set the DC voltage back to the reference value. However, this post fault behaviour is only valid numerically speaking. In the real world the B2B would have disconnected as a last protection measurement to safeguard the integrity of the DC elements of the system.

In order to protect the DC capacitor from transient over voltages, a new control technique is needed where, in case the GSC cannot deliver to the grid the power in the DC bus, then the MSC should decrease or even stop its power injection to the DC grid. To achieve this objective, new control loop is added to the MSC active power control. This control loop is activated when the DC voltage goes beyond a safety limit and commands the active power control loop to reduce the active power set point in a manner proportional of the rate of

change of the DC voltage. Mathematically, the dynamics of the DC voltage in the B2B converter can be described as:

$$\frac{C}{2} \frac{dv_{dc}^2}{dt} = P_{MSC} - P_{GSC} \tag{46}$$

where  $P_{MSC}$  is the active power coming from the MSC and  $P_{GSC}$  is the active power of the GSC. As such the rate of change of the DC voltage is an indication of the amount of power mismatch between GSC and MSC. Therefore, if the rate of change of the DC voltage is used, an estimation of the amount of power reduction of MSC to limit the transient overvoltage is obtained. Calculating this rate of change implies the derivation of the DC voltage signal which will become overly noisy if without any pre-filtering. However, if a filter of the right cut out frequency is selected then the signal from the derivation of the DC voltage can be used to regulate the power reference of the MSC. This approach was constructed in Simulink and incorporated to the MSC controllers. A schematic diagram of the new controller is shown in Figure 44.

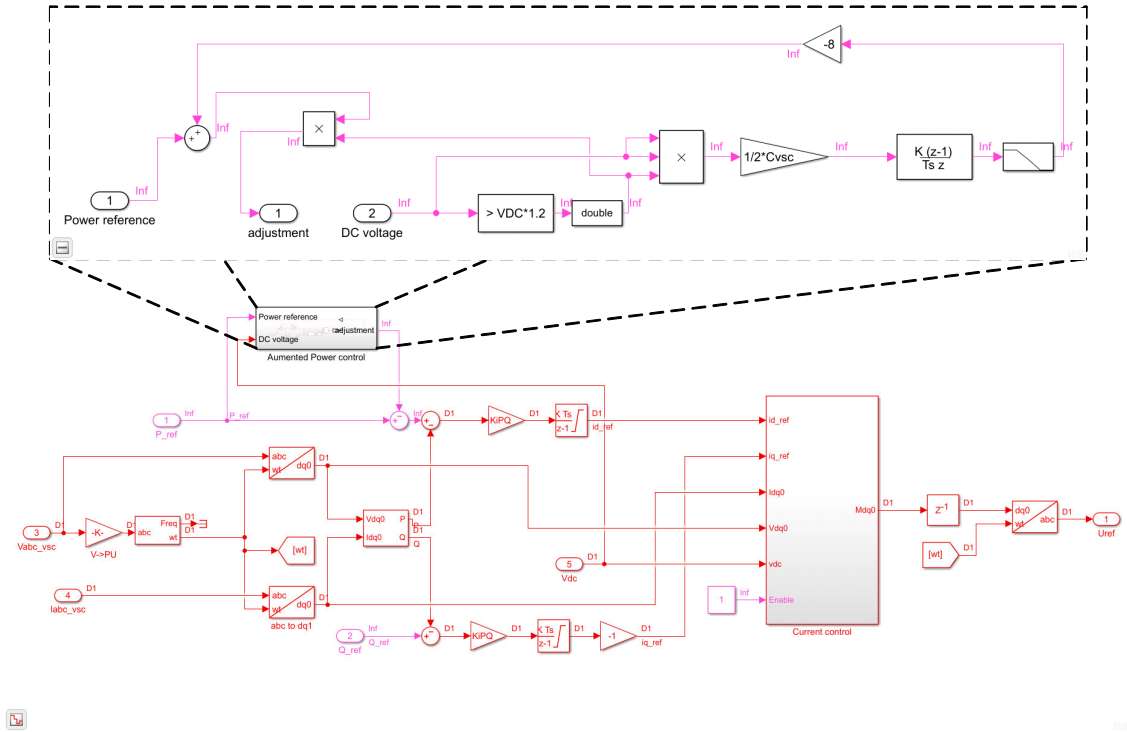


Figure 44: Inclusion of advanced MSC power reference controller for adding fault ride-through capabilities to the B2B converter.

As seen in Figure 44, the new active power reference controller is added to the controllers of the MSC. The active power reference controller, activates whenever the DC voltage goes beyond 1.2 PU in value, when that happens, an active power set point reduction is enforced. This reduction is proportional to the rate of change of the DC voltage, meaning that steeper voltage increases will trigger a higher reduction of the active power set point. The magnitude of the power reduction can be further amplified by a gain for extra protection.

Figure 45 shows the behaviour of the MSC and GSC for the same fault condition but this time with the addition of the active power reference controller to limit the overvoltage in the DC link. As seen in Figure 45 f), the DC voltage of B2B converter is kept below 60kV during the fault, which is considered a safe value for the device. The effects of the additional active power reference controller can be seen in the AC power of the MSC in Figure 45 a), where it can be noticed that the active power of the MSC is actively reduced following the rate of change of the DC voltage. After the fault is cleared, the GSC is able to take the DC voltage back to its original set point and the active power reference of the MSC is back to pre-fault levels.

The implications of using an active power reference controller to reduce overvoltages imply subjecting the flexible hydro transformer to power oscillations. However, these types of oscillations are the same the generator would see if it would be connected directly to the AC network during a fault. Future controller developments, both in the B2B converter and the flexible hydro generator, will need to be created to enable a full fault ride-through capability of the Hydro-B2B system.

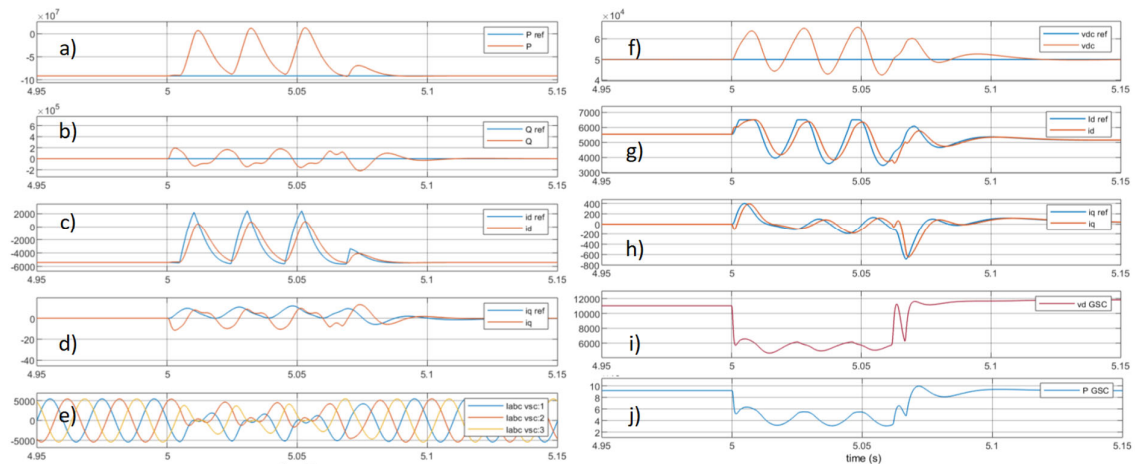


Figure 45: MSC and GSC behaviour during an event of a 3 phase fault at AC grid, a) MSC active power, b) MSC reactive power, c) MSC d current, d) MSC q current, e) MSC abc currents f) GSC DC voltage, g)GSC id current, h)GSC iq current, i)GSC v-d of AC grid j) Active power of the GSC

## 4. Conclusions

This work reported the development of a multi machine AC network for testing of dynamic conditions in AC systems. The developed AC grid was interfaced with a B2B converter modelled with robust controllers for extra stability under severe dynamic grid conditions.

The developed network was able to provide simulations of dynamic situations of different type and intensity. This multi-machine AC grid will be useful for the design of advanced controllers for the B2B converter that provide ancillary services to the grid and full fault ride through capabilities.

The B2B converter controller was designed with the capability to reject disturbances and synchronize with the AC grid even during extreme dynamic AC conditions. The converter controller robustness already allowed the deployment of yet another extra control loop to increase the fault ride through capabilities of the system. This proves the usefulness of the model for future controller design iteration where more complex dynamic interaction, such as the full model of the flexible hydro generator is connected to the B2B converter.

## 5. References

- [1] S. Lumbreras and A. Ramos, "Offshore wind farm electrical design: a review," *Wind Energy*, vol. 16, no. 3, pp. 459-473, 2013.
- [2] R. Srikakulapu and U. Vinatha, "Electrical collector topologies for offshore wind power plants: A survey," in *2015 IEEE 10th International Conference on Industrial and Information Systems (ICIIS)*, 2015, pp. 338-343.
- [3] C. Hsin-Ju, G. L. Kusic, and G. F. Reed, "Comparative PSCAD and Matlab/Simulink simulation models of power losses for SiC MOSFET and Si IGBT devices," in *2012 IEEE Power and Energy Conference at Illinois*, 2012, pp. 1-5.
- [4] *Power System Stability And Control*. McGraw-Hill, 1994.
- [5] A. A. Ba-muqabel and M. A. Abido, "Review of conventional power system stabilizer design methods," in *2006 IEEE GCC Conference (GCC)*, 2006, pp. 1-7.
- [6] C.-M. Ong, "6.8 Simulation of an induction machine on the stationary reference frame," in *Dynamic Simulations of Electric Machinery: Using MATLAB/SIMULINK*: Prentice Hall PTR 1998, p. 196.
- [7] M. Ciobotaru, R. Teodorescu, and F. Blaabjerg, "A new single-phase PLL structure based on second order generalized integrator," in *2006 37th IEEE Power Electronics Specialists Conference*, 2006, pp. 1-6.
- [8] D. Campos-Gaona, E. L. Moreno-Goytia, and O. Anaya-Lara, "Fault Ride-Through Improvement of DFIG-WT by Integrating a Two-Degrees-of-Freedom Internal Model Control," *Industrial Electronics, IEEE Transactions on*, vol. 60, no. 3, pp. 1133-1145, 2013.
- [9] M. Morari and E. Zafiriou, *Robust Process Control*. New Jersey: Prentice-Hall, 1989.
- [10] T. H. Lee, T. S. Low, A. Al-Mamun, and C. H. Tan, "Internal model control (IMC) approach for designing disk drive servo-controller," *Industrial Electronics, IEEE Transactions on*, vol. 42, no. 3, pp. 248-256, 1995.
- [11] D. Campos-Gaona, R. Peña-Alzola, and M. Ordonez, "Nonminimum Phase Compensation in VSC-HVDC Systems for Fast Direct Voltage Control," *IEEE Transactions on Power Delivery*, vol. 30, no. 6, pp. 2535-2543, 2015.
- [12] A. Yazdani and R. Iravani, *Voltage-Sourced Converters in Power Systems: Modeling, Control, and Applications*. Wiley, 2010.
- [13] R. Ottersten, "On the Control of Back-to-Back Converters and Sensorless Induction Machine Drives," PhD Thesis, Department of Electric Power Engineering, Chalmers University of Technology, Göteborg, Sweden, 2003.